Thermal conductivity of an Fe-Ni alloy and implications for heat flow in the cores of terrestrial bodies

By:

Alex Vanderhoeff

Supervisor:

Dr. Richard Secco

A thesis submitted in partial fulfilment
of the requirements for the degree of
Bachelor of Science (BSc),
Honours Specialization in Geophysics

Department of Earth Sciences
The University *of* Western Ontario
London, Ontario, Canada
April 22, 2020

Abstract

Earth's geomagnetic field is driven by the geodynamo. The geodynamo today is driven by vigorous convection in the outer core (OC) due to compositional convection. Compositional convection is caused by inner core (IC) crystallization. This forces the onset of compositional convection to be the age of the IC, with some estimates ranging from 0.5-1 Ga. Paleomagnetic evidence shows the geomagnetic field has persisted since 3.5-4.2 Ga which is at odds with the IC age. This requires another source of energy to drive the geodynamo and thermal convection is the most investigated candidate. Compositional convection can only occur if the thermal conductivity (k) of the OC material is low enough, since heat is conducted first, and the excess heat is convected. If k is too high, all heat is conducted to the Core-Mantle Boundary (CMB), and no thermal convection can occur. This makes k of the OC materials critically important for the Earth and other terrestrial bodies.

In this project, I experimentally determined electrical resistivity of Fe10Ni at 3-5 GPa and at high temperatures using a 1000-ton cubic anvil press. At 4 GPa, the electrical resistivity was measured in the melt phase. I then calculated the thermal conductivity of the alloy from the electrical resistivity using the Wiedemann-Franz law. Using the thermal conductivity, the heat flow at the top of the lunar core was calculated. The thermal conductivity at 4 GPa in the melt for Fe10Ni was determined to be 32 W/(mK). The data could not be extrapolated to Earth CMB pressure without more data points above the melt, so heat flow to the Earth's CMB was not calculated. Using this 4 GPa data, the adiabatic heat flow at the top of the lunar OC was calculated, since the experimentally determined values are near lunar OC pressures and temperatures, so large extrapolations were unnecessary. The adiabatic heat flow at the top of the lunar OC was calculated to be 1.5-3.0 mW/m^2. This is lower than values calculated with pure iron, and also lower than estimates of heat flux through the lunar CMB which indicates thermal convection may have occurred to drive the lunar magnetic field during the lunar magnetic era ending 3.7-3.45 Ga.

Acknowledgements

I would first and foremost like to thank my supervisor, Dr. Richard Secco, for providing the guidance, encouragement and aid necessary to complete the project.

I would also like to thank Dr. Wenjun Yong, Joshua Littleton, Meryem Berrada and Dr. Yilong Pan for assistance with preparing parts and designs for the cells, along with providing valuable advice and guidance throughout the project.

I would also like to thank Jon Jacobs for teaching me the art of machining and his assistance with preparing parts for the experiments.

Table of contents

List of figures

List of Tables

Chapter 1: Introduction

1.1: Composition of the core

The Earth's geomagnetic field is generated through vigorous convection in the liquid outer core (OC). This OC consists of mostly Iron (Fe), with about 5-15wt% Nickel (Ni) and 5-15wt% light elements such as Sulfur (S), Silicon (Si), Oxygen (O), and Carbon (C) (McDonough and Sun, 1995). The exact composition cannot be determined at the present time with the mineral physics and seismological data that are currently available (McDonough and Sun, 1995). The evidence for this approximate core composition comes from sources from several different fields. Seismological data show that the seismic velocity of the outer core has a similar value to calculated seismic velocity values for Fe-Ni alloyed with the light elements suggested by McDonough and Sun (Davies et al., 2015). Data from iron meteorites, thought to originate from the cores of differentiated terrestrial bodies, give evidence for Fe and Ni in Earth's core and a range of possible amounts of each. The outer core also must be a good electrical conductor, as is Fe, to be able to generate the electrical currents necessary for the geodynamo mechanism to occur. The density of the core provides further evidence for Fe in the core via the Adams – Williamson equation, which gives the density change of the earth with depth. Calculations using the Adams - Williamson equation showed the core needs to be composed of denser materials than silicates in order to achieve the known average density of Earth of 5.5 g/cm^3, so Fe was suggested (Williamson and Adams, 1923). Spectroscopic data from the solar photosphere give abundances of elements in the solar system and the expected total amount of Fe in the Earth can be accounted for if Fe is the main core material.

1.2: Convection in the outer core

The geomagnetic field is maintained when the magnetic diffusion is balanced by the generation of new magnetic field through magnetic induction (Stevenson, 2003). For the magnetic field to become induced by electrical currents in the outer core, the fluid must be moving. The fluid moves in convection cells throughout the outer core. The cause of convection is through gravitational instabilities due to buoyancy differences in the fluid. In the outer core today, the main form of convection occurring is called compositional or chemical convection. This form of convection occurs because of the secular cooling of the outer core (Stevenson, 2003). When the outer core temperature reaches the solidus of the Fe alloy composing the outer core, the Fe alloy freezes out of the melt. The structure of the Fe when it freezes out is hexagonal – closely packed (HCP) Fe, which is the dominant phase of Fe at inner core (IC) conditions (Tateno et al., 2010). This freezing out occurs near the Inner Core Boundary (ICB). As the Fe alloy cools, the crystals are denser than the surrounding fluid due to volume reduction of the phase change and light element partitioning (Zhang et al., 2019). The light elements in the core (possibly Si, S, C, O) are fractionally preferred into liquid (Fearn and Loper, 1981). Metallurgical studies show that when a solid material freezes out of a melt, the heavy component is preferred into the solid (Chalmers, 1964). As a result, there is a higher concentration of light elements locally. The heavy elements then sink and form the F layer at the base of the outer core (Zhang et al., 2019). The F layer is a slurry layer with a mix of melt and solid. The solid Fe then reaches the bottom of the F layer. As more solid Fe alloy reaches the bottom of the F layer, it starts to pile. Once the Fe alloy is sufficiently packed, it forms a new layer called the F’ layer. As the solid Fe alloy is sinking to the base of the F layer, the melt with a higher concentration of light elements rises due to the lower density. This rising melt is what drives compositional convection.

Convection in the outer core is largely occurring at the present time due to compositional convection. Because compositional convection occurs from secular cooling of the core, it could only have occurred when Fe started to solidify from melt and form the inner core. This gives the inner core a maximum age. The inner core must have started to form when compositional convection started to occur and must then be the same age. The age of the inner core has been estimated to be as young as 0.5 Ga (Gomi et al., 2013; Labrosse, 2015) to nearly primordial (Stacey and Loper, 2007). The age of the inner core estimates contrasts with the age of the geomagnetic field, which paleomagnetic evidence has found to be between 3.5 Ga (Biggins et al., 2011) and 4.2 Ga (Tarduno et al., 2015). This means that there must have been another method of convection occurring for the geomagnetic field to be generated by the geodynamo.

Another form of convection potentially occurring in the outer core is thermal convection. This form of convection occurs due to buoyancy differences from heating of localized melt. Primordial heat from accretion and differentiation of the earth, the latent heat of crystallization of the iron and nickel out of the melt and possibly from the radioactive decay of radiogenic isotopes such as potassium (K), uranium (U), and thorium (Th) are the energy sources for the Earth’s heat budget. An outer core that is heated from below (by transfer of IC heat outward) is the cause of OC thermal convection (Stevenson, 2003).

1.3: Heat flow from the core

The mantle acts as a heat sink for the outer core. Heat is transferred through the outer core towards the Core-Mantle Boundary (CMB) by conduction through an adiabatic temperature gradient, as well as possibly thermal convection. The mantle can only accept a finite amount of heat from the outer core across the CMB. The amount of heat the mantle accepts from the outer core depends on mantle convection which removes heat from the CMB and distributes it upwards (Davies, 2016). Estimates for the heat flow used to be 3-4 TW across the CMB (Stacey and Loper, 1983), but recent estimates are much larger at 5-15 TW (Lay et al., 2008). This means the total heat flux across the CMB can be a maximum of 15 TW by these estimates and is through conduction across the CMB. Heat is transported by a combination of convection and through conduction along an adiabatic temperature gradient in the OC (Gubbins et al., 2015). The adiabatic temperature gradient in the OC, $\frac{(\partial T)}{(\partial r)_S}$, where T is the temperature and r is the radius, is given by (Anderson, 1998):

$$\frac{(\partial T)}{(\partial r)_S} = -\frac{gT\gamma}{\phi} \tag{1}$$

where g is gravitational acceleration, T is temperature, γ is Gruneissen's parameter, which is 1.3 in the liquid outer core (Anderson, 1998) but is 1.5 in some newer estimates (Gubbins et al., 2015), and ϕ is the seismic parameter.

The outer core can conduct heat along the adiabatic temperature gradient through electron conduction (k_e) and phonon conduction (k_{ph}). Thermal convection can only carry heat in excess of the heat conducted down the core adiabat (Stacey and Anderson, 2003). This makes the property governing how much heat is conducted down the adiabat to the CMB, the thermal conductivity (*k*) of the outer core, a critically important value. The thermal conductivity value determines if thermal convection is occurring in the outer core. This is because the outer core transports heat to the mantle, and the mantle can only accept a finite amount of heat (Davies et al., 2015). If the mantle can only accept 5-15 TW (Lay et al., 2008), and if the outer core has a high thermal conductivity, such as the 90-150 W/(mK) recently measured and calculated by Gomi et al (2013) and de Koker et al (2012), respectively, then all the heat will be transferred to the CMB from the ICB (i.e. through the OC) through thermal conduction down the adiabat and there could be no thermal convection. These high *k* values force the inner core to be young, since the heat removal from the outer core is faster, causing the inner core to cool faster. If the thermal conductivity is a lower value (e.g. 22 W/(mK) such as estimated by Stacey and Loper, 2007), then the inner core is old, and the secular cooling of the core has been slower. With a lower thermal conductivity value such as this, thermal convection and thermal conduction could both be the heat transport mechanisms in the outer core. If there is no thermal convection occurring in the outer core, there is no method for convection in the core before the inner core started to form, meaning there cannot be a geomagnetic field, which is at odds with paleomagnetic evidence (Olson, 2013). This raises questions as to how the geomagnetic field has been generated if the inner core is young.

1.4: Radioactivity of the core

If there is a large amount of radiogenic elements in the core producing heat in the outer core, then the core would have cooled more slowly and there could be thermal convection of the outer core to sustain the geodynamo before IC solidification. There have been several studies that explored the possibility of radiogenic potassium (K) in the outer core. It has been found that K behaves like a transition element and can enter the Fe lattice (Bukowinski, 1976) and that it can alloy with Fe at > 26GPa and > 2500K, which could imply it can alloy at high pressures and temperatures. There has been no evidence of K or other radiogenic isotopes in iron meteorites (Buchwald, 1975), although this could be because the bodies from which the meteorite originated from did not have high enough pressures and temperatures for K to enter the lattice (Bukowinski, 1976). Adding a few hundred parts per million of K to the outer core has also been shown to extend the age of the inner core by 100 – 300 million years (Nimmo, 2015; Labrosse, 2015). The amount of K estimated to be in the core has varied depending on the estimate for the thermal conductivity of the outer core, since if low enough (around 20 W/(mK)) there would be no need for radiogenic isotopes (Nimmo, 2004). The large range in values for the thermal conductivity of the core means that the viability of radiogenic isotopes in the outer core cannot be determined until the thermal conductivity value is agreed upon.

1.5: Thermal conductivity and electrical resistivity of metals

There are two mechanisms of thermal conduction in a material. Phonon conduction (k_{ph}) result from quantized lattice vibrations that can transport energy via vibrational waves (Kittel, 2005). Thermal conductivity through phonon conduction scales as the inverse of temperature, with lower phonon conduction at higher temperatures. This inverse relationship between temperature and phonon conduction is caused by phonon scattering. There is also electron conduction (k_e), where electrons conduct heat as well as charge due to the mobility of electrons. Electrons can be scattered through electron – electron scattering, electron – phonon scattering and electron – impurity scattering. Electrons can also be impeded through interactions with spin disorder (magnons) associated with transition metal ions (Drchal et al., 2017). Electron – phonon scattering is thought to be more dominant at OC conditions according to some studies (e.g. Gomi et al., 2013; Gomi et al., 2015). Some newer studies by Xu et al (2018) and Pourovskii et al (2017) disagree with this and find electron – electron scattering to be significant at high temperatures.

In insulators, k_{ph} is dominant because electrons are less mobile. In a transition metal such as Fe, electrons have more mobility due to the weak binding of the valence electrons (Kittel, 2005). This makes k_e dominant in metals and a highly effective transporter of heat (Kittel, 2005). In a metal, k_e is coupled with electrical resistivity, ρ (Uher, 2004), and k_e is inversely proportional to the ρ. This relationship is given by the Wiedemann – Franz law (WFL) (Wiedemann and Franz, 1853):

$$k_e = \frac{LT}{\rho} \tag{2}$$

where T is temperature, ρ is the electrical resistivity and L is the Lorenz number, with the Sommerfeld value of the Lorenz number usually used, $L=2.44 \times 10^{-8}$ WΩ/K^2. The WFL is more of a correlation and less of a law, as it is an empirically-based approximation. The WFL allows the calculation of k_e from the electrical resistivity of a material. Since $k = k_e + k_{ph}$, the WFL is thought to give the lower limit for the thermal conductivity (Secco, 2017), since only k_e is determined from it. Since k_e is dominant in the outer core, it is still a good estimate. A recent study by Watanabe et al (2019) measured thermal conductivity of Fe-Ni melts at 1 atm and measured values larger than those found by using electrical resistivity and the WFL to calculate thermal conductivity. This could imply that the k_{ph} contribution to thermal conductivity is larger than previously thought, in contradiction to previous estimates of the contribution of k_{ph}. The Sommerfeld value was found by Secco (2017) to represent 99% of the electronic component of thermal conduction for pure Fe. The WFL is widely used to calculate the thermal conductivity of outer core compositions, since measuring the thermal conductivity of a material at the high pressures and high temperatures of the core is experimentally difficult. In experiments that have done so, the measurements typically have large measurement errors. This is because a well controlled temperature gradient over a very small and highly conductive sample must be kept for an accurate measure of the heat flow (Secco, 2017). The more easily measured electrical resistivity can be obtained and then thermal conductivity can be calculated with the WFL. The Sommerfeld value of the Lorenz number is a theoretically derived value (Uher, 2004). It is the free electron value of the Lorenz number. The Sommerfeld value of the Lorenz number assumes that electrons will have minimal interaction with metal ions (Uher, 2004). Pourovskii et al (2017) found through density functional theory (DFT) and dynamical mean-field theory (DMFT) calculations that Fermi – liquid (FL) like behaviour can be present in HCP Fe up to IC conditions. In FLs, the WFL could provide an overestimation of the thermal conductivity because the Lorenz number is suppressed by inelastic electron – electron collisions which are more extensive in FLs (Pourovskii et al., 2017). They also found a Lorenz number in this situation to be 1.589×10^{-8} WΩ/K^2, significantly smaller than the Sommerfeld value. Gomi et al (2015) determined that the electronic component of thermal conduction is dominant, and that inelastic scattering is likely negligible at high temperatures, in disagreement with Pourovskii et al (2017). Xu et al (2018) disagrees that Fe behaves in a FL fashion at high temperatures, although they find significant contributions from electron – electron scattering at high temperatures. Xu et al estimated a value of the Lorenz number to be 2.10 – 2.15 x 10^{-8} WΩ/K^2 from the CMB to the ICB. This value is lower than the Sommerfeld value of the Lorenz number. Secco (2017) used a multi anvil press to experimentally determine if the Sommerfeld value of the Lorenz number allows the thermal conductivity to be estimated adequately for Fe and Fe-Si. It was found that the Sommerfeld value underestimates the thermal conductivity for Fe-Si above the melting point (Secco, 2017). For Fe above the melting point, while the Sommerfeld value of Fe can be justified, it was still found that there is a non-negligible component of k_{ph} for which the Sommerfeld value does not account (Secco, 2017). The disagreement as to the validity of the Sommerfeld value for different outer core compositions indicate that further study is needed. Continued efforts need to be made to determine whether electron – electron scattering is elastic or inelastic in nature. If it is elastic, energy is conserved and the WFL will hold and provide a good estimation (Pourovskii et al., 2017). If the scattering is inelastic in nature, then heat can be lost in the collision, decoupling the electrical resistivity and thermal conductivity transport properties and make the WFL inaccurate (Williams, 2018).

Electron – impurity scattering is difficult to assess and has large implications for the electrical resistivity due to the OC material likely being an Fe alloy with Ni and light elements (Williams, 2018). More impurities alloyed with Fe raises the electrical resistivity, lowering the thermal conductivity. Gomi et al (2013) and Gomi et al (2015) used Matthiessen's rule, which states the resistivity of the impurities are additive:

$$\rho_{mix}(V,T) = \rho_{Fe}(V,T) + \sum \rho_i(V) X_i \tag{3}$$

where ρ_{mix} is the total resistivity, ρ_{Fe} is the resistivity of Fe, ρ_i is the resistivity of each impurity *i (i=1…n),* and X_i is the molar concentration of impurity components. There is a breakdown of Matthiessen's rule when the resistivity is very high, such as at high temperatures that would be found in the OC. The resistivity shows a saturation behaviour at these high resistivity conditions called saturation resistivity (Gunnarsson et al., 2003; Gomi et al., 2013). Resistivity saturation is when the resistivity saturates and grows slower with increasing temperature (Gomi et al., 2013). This is because the mean free path, ℓ**,** that an electron travels before it collides with another electron or particle and scatters gets smaller. This happens in most metals and is because the mean free path distance, ℓ, approaches the inter – atomic distance, d**.** This is described by the Ioffe – Regel condition**:** ℓ ≥ d (Ioffe and Regel, 1960). When this is violated, the metal has reached resistivity saturation and the resistivity ceases to increase (Gomi et al., 2013). This inter – atomic distance could grow smaller due to higher pressures, which would cause lower resistivity and consequently higher thermal conductivity. Calculations accounting for the resistivity saturation at high temperatures (Gomi et al., (2013), Gomi et al., (2015); Ohta et al., (2016)) found much higher thermal conductivity values than those that did not (Seagle et al., (2013)).

Temperature and pressure also affect the electrical resistivity of a metal. A higher temperature means more phonons will be present, making electron – phonon scattering more likely and raising the electrical resistivity or inversely lowering the thermal conductivity (Stacey and Anderson, 2001). Pressure reduces the amplitude of the phonons and reduces the electrical resistivity, raising the thermal conductivity.

1.6: Past studies on thermal conductivity and electrical resistivity of outer core materials

Estimates and calculations of the thermal conductivity and electrical resistivity of the Earth's core started when Elsasser (1946) calculated an electrical resistivity value for the OC of 2.0 x 10^{-6} Ωm, neglecting the effect of Fe alloying. This was done by considering resistivity proportional to temperature, and inversely proportional to the square of the Debye temperature. In 1948, Bullard calculated the electrical resistivity of Fe, accounting for impurity effects from Ni alloying, pressure and temperature. He then averaged his value with Elsasser's to get an electrical resistivity of 3.0 x 10^{-6} Ω m (Bullard, 1948). The averaged value of Bullard was widely used until Gardiner and Stacey (1971) calculated the electrical resistivity to be 2.59-3.19 x 10^{-6} Ω m at the CMB and 2.62-3.25 x 10^{-6} Ω m at the ICB. Jain and Evans (1972) then calculated the electrical resistivity of pure liquid iron and found it to be 1.04 $\pm$ 0.06 x 10^{-6} Ω m for the CMB and 1.0-2.0 x10^{-6} Ω m when accounting for alloying of Fe with Ni at CMB conditions. Matassov (1977) then performed shock compression experiments on Fe-Si alloys (7.7 - 34.2 at% Si) at 5-140 GPa and temperatures of 670-2700 K and found the electrical resistivity of the core to be 1.15 x 10^{-6} Ω m. Secco and Schloessin (1989) carried out static high-pressure high temperature experiments on pure liquid Fe using a 1000-ton cubic anvil press up to 7 GPa and temperatures above the melting point of liquid Fe. They estimated the electrical resistivity to be 1.2 - 1.5 x 10^{-6} Ω m. Stacey and Anderson (2001) used the electrical resistivity measurements of Matassov (1977) to estimate the electrical resistivity of the outer core. They accounted for the effect of impurity resistivity of Ni and Si and calculated the electrical resistivity to be 2.12 x10^{-6} Ω m at the CMB and 2.02 x10^{-6} Ω m for the ICB. This corresponds to thermal conductivity values of 46 W/(mK) and 63 W/(mK) respectively. They also found that for a pure metal, the temperature and pressure effects can be represented by constant resistivity on the melting curve. This has been found to be true in experiments with Ni using a multi anvil press up to 9 GPa (Silber et al., 2017) and for experiments with Fe above the triple point at 5.2 GPa using a multi anvil press up to 12 GPa (Silber et al., 2018) and 24 GPa (Yong et al., 2019). Bi et al (2002) then found that the epoxy that encapsulated the samples in previous shock wave measurements of the electrical resistivity such as by Matassov (1977) becomes electrically conductive at high pressures above 50 GPa. This leads to shunting of the Fe samples and larger thermal conductivity values (Bi et al., 2002). Stacey and Loper (2007) then revised the electrical resistivity estimate by Stacey and Anderson (2001) to $3.62 \times 10^{-6}\ \Omega$ m with a corresponding thermal conductivity of 28-29 W/(mK) almost uniformly throughout the outer core. This low value for the thermal conductivity was found to provide enough heat to power the geodynamo through thermal convection for 3.8 Ga and if *k* were present with an output of 0.2 TW, power the geodynamo for 4.5 Ga. This value by Stacey and Loper (2007) was the commonly accepted value for the thermal conductivity of the outer core until 2012, when de Koker et al (2012) used ab initio molecular dynamics (MD) calculations to determine the electrical conductivity of liquid Fe and liquid Fe-Si. They found a thermal conductivity of 215 W/(mK) for Fe, 156 W/(mK) for Fe with 25 wt% Si (Fe25Si) and 218 W/(mK) for Fe12.5O. These thermal conductivity values are a factor of 5-10 higher than Stacey and Loper's values. These thermal conductivity values gave a heat flux to the top of the outer core of 14-20 TW, much larger than the 5-15 TW that the mantle will accept from the OC (de Koker et al., 2012). Pozzo et al (2012) also calculated the thermal conductivity of pure Fe liquid using ab initio molecular dynamics simulations. They found the thermal conductivity at the CMB to be 140-144W/(mK) and 215 – 223 W/(mK) for pure liquid Fe at the ICB. These two studies show drastic changes in the value of the thermal conductivity from Stacey and Loper (2007) and correspond to a young inner core of 0.5-1 Ga. Gomi et al (2013) experimentally measured the electrical resistivity of pure solid Fe up to 100 GPa and room temperatures using a diamond anvil cell press (DAC). The temperature dependence was then extrapolated for using the Bloch – Gruneisen (BG) equation. The study then accounted for impurity resistivity of an Fe-Si alloy and considered resistivity saturation. This was the first study measuring or calculating electrical resistivity of the core to account for resistivity saturation. The WFL was then used to calculate the electronic component of the thermal conductivity. The Sommerfeld value of the Lorenz number was used in the calculation. Accounting for resistivity saturation greatly reduced the electrical resistivity of the pure Fe, thus giving a much larger value for the thermal conductivity, 90 W/(mK) at the CMB and 148 W/(mK) for the ICB of an Fe-Si alloy (Gomi et al., 2013). Gomi et al also found a sharp jump in the electrical resistivity of Fe due to a phase change from body-centred cubic (BCC) to HCP Fe at about 15 GPa. Seagle et al (2013) then measured the electrical resistivity and calculated the thermal conductivity of solid Fe and solid Fe-Si to 60 GPa and room temperature. They found a similar jump due to phase change from BCC to HCP of Fe at about 13 GPa. Seagle et al (2013) did not account for resistivity saturation. For pure Fe, they found a thermal conductivity of 67 – 145 W/(mK) and for Fe9Si a thermal conductivity of 41-60 W/(mK). The effect of the impurity resistivity was calculated using Matthiessen's law. The Sommerfeld value of the Lorenz number was used in the WFL calculation. Gomi et al (2015) used a DAC experiment to measure the electrical resistivity of Fe-Ni alloys of 5, 10 and 15% Ni at up to 70 GPa and ambient temperatures. They then used the BG equation to extrapolate for temperature and extrapolated for pressure to core conditions. They also accounted for resistivity saturation in their calculations using the shunt resistor model given by:

$$\frac{1}{\rho_{tot}(V,T)} = \frac{1}{\rho_{ideal}} + \frac{1}{\rho_{sat}} \qquad (4)$$

where ρ_{ideal} is the ideal resistivity with no resistivity saturation described by Matthiessen's rule, ρ_{sat} is the resistivity saturation of Ni and $\rho_{tot}(V,T)$ is the total resistivity of the sample (Gomi et al., 2015). Gomi et al (2015) found that the impurity resistivity of Ni increased linearly with increasing Ni concentration at ambient temperature. Gomi et al (2015) found that the resistivity saturation at higher extrapolated temperatures has a significant effect on the electrical resistivity. It caused the resistivity impurity to saturate regardless of the resistivity impurity of the Ni. The impurity resistivity of the Ni is given by:

$$\rho_{Ni}(V) = 7.25x\left(3.51 - \frac{V}{V_0}\right)^{-8.06} x10^{-5}(\Omega m/at\%) \qquad (5)$$

With ρ_{Ni} being the impurity resistivity of Ni and V_0 and V are the lattice volume at 1 atm and high pressure, respectively . Stacey and Anderson (2001) estimated the impurity resistivity for 10 atomic % Ni to be 1.5 x 10^{-7} Ωm. Ohta et al (2016) then measured the electrical resistivity of solid Fe using a laser-heated DAC (4490 K, 157 GPa) and DAC with low-temperature external heating source (450 K, 212 GPa). To convert the measured value of the electrical resistivity to liquid Fe at core conditions, Ohta et al (2016) used a resistivity saturation model to fit their data. They then used the BG equation to extrapolate for the effect of temperature. They found that their data showed lower electrical resistivity values than the extrapolations using the BG formula and think this may be because of resistivity saturation on the resistivity at high temperatures and pressures. The effect of impurity resistivity of 10% Ni and 22.5% Si was accounted for in the model using Matthiessen's rule (Ohta et al., 2016). They also included the effect of melting on the resistivity, by assuming a 20% increase in electrical resistivity due to melting. Using the WFL with the Sommerfeld value of the Lorenz number on the electrical resistivity data, they found the outer core thermal conductivity of the Fe10Ni22.5Si alloy to be 88 W/(mK) (Ohta et al., 2016). This thermal conductivity value gives an inner core age of as little as 0.7 Ga (Ohta et al., 2016). Another study by Konôpková et al (2016) is a stark contrast to the estimate by Ohta et al (2016). In the study by Konôpková et al (2016), the thermal conductivity of solid Fe was measured directly at high temperatures and pressures in a laser-heated DAC. They directly measured thermal conductivity by monitoring the heat pulse from a nanosecond laser propagate through the Fe sample. The time taken for the pulse to pass from the laser-heated side to the other side and the amplitude difference of the pulse between sides are functions of the sample's thermal conductivity. They then used finite-element modelling of the temperature field in the DAC. The changes in brightness and wavelength of the glow gave a thermal conductivity value of 25 ± 7 W/(mK) at the CMB and 35 ± 10 W/(mK) at the ICB (Konôpková et al., 2016). The effect of melting was not considered in these values, but an effect of impurity resistivity lowering the thermal conductivity by 10-40% was accounted for (Konôpková et al., 2016). These values for the thermal conductivity of the core allows for the geodynamo to be sustained for the whole life of the planet because the excess of the adiabatic (conducted) heat would have been transported by thermal convection, thereby driving the geodynamo (Konôpková et al., 2016). Xu et al (2018) conducted ab initio MD calculations using DFT. They calculated a thermal conductivity value of 77 W/(mK) that is consistent with thermal convection occurring and an older inner core. Xu et al (2018) accounted for the effect of electron-electron scattering and electron – phonon scattering. Studies by Pozzo et al (2012) and de Koker et al (2012) accounted only for electron – phonon conduction in their computations (Xu et al., 2018). The following table summarizes estimates of the thermal conductivity at high pressures and temperature.

Table 1.1: Summary of thermal conductivity values from recent studies (Secco, 2017).

COMPOSITION	**P (GPa)**	**T (K)**	**k_e (W/mK)**	**Method**	**Comment**	**REFERENCE**
Fe	325	6000	215	C	N/A	De koker et al., 2012
Fe	136	3750	67-145	E_ρ	Experiments at room temperature, extrapolated to high temperature.	Seagle et al., 2013
Fe	140	3750	226	E_ρ	N/A	Ohta et al., 2016
Fe	136	3800	33	E_k	Direct k measurement.	Konôpková et al., 2016
Liquid Fe alloy	OC conditions	OC conditions	77	C	N/A	Xu et al., 2018
Fe25Si	329	5000	22	C	Used data collected by Matassov, 1977.	Stacey and Loper, 2007
Fe25Si	325	6000	156	C	N/A	De koker et al., 2012
Fe22Si	135	3750	90	E_ρ	Experiments at room temperature,	Gomi et al., 2013

					extrapolated to high temperature.	
Fe22Si	330	4970	148	E_ρ	Experiments at room temperature, extrapolated to high temperature.	Gomi et al., 2013
Fe9Si	136	3750	41-60	E_ρ	Experiments at room temperature, extrapolated to high temperature	Seagle et al., 2013

E_ρ- Experimental study, measuring electrical resistivity and using WFL to calculate thermal conductivity.

E_k- Experimental study, measuring the total thermal conductivity at high pressure and temperature.

C- Computational study.

1.7: The lunar core

The thermal conductivity data to be measured in this study will be applicable to calculations of the heat flow at the top of the lunar core. Since the pressure at the top of the liquid lunar OC is 4.8 GPa (Garcia et al., 2012) and the press used in this study has a maximum of 5 GPa pressure. Hence, the electrical resistivity and thermal conductivity measured in this study are representative of lunar OC conditions. Based on paleomagnetic intensity data, the Moon is thought to have had a strong magnetic field of around 110 µT (Wieczorek et al., 2006) between 4.2-3.56 Ga ago (Garrick-Bethell et al., 2009; Shea et al., 2012; Suavet et al., 2013). This magnetic field could have been generated due to dynamo action in the moon driven by thermal or compositional convection, as is occurring now in the Earth. Another possible mechanism to generate energy to drive the dynamo could include stirring of the liquid OC caused by the differential motion between the solid lunar mantle and the liquid lunar OC (Dwyer et al., 2012). It is thought that thermal convection was an important mechanism to stir the lunar OC due to high temperatures and a very young or non-existent IC (Scheinberg et al., 2015). In order for thermal convection to occur, the heat transferred by the adiabatic heat flux, q_{ad}, at the top of the core must have been less than the total heat flux across the lunar CMB.

1.8: Purpose of this study

This study seeks to measure the electrical resistivity of Fe10Ni alloy at high pressures and temperatures above its melting point using a 1000-ton cubic anvil press. This study also seeks to determine if Fe- Ni alloys have constant electrical resistivity along their melting curves as has been shown for Fe and Ni individually (Silber et al., (2017); Silber et al., (2018); Yong et al., (2019)). If the electrical resistivity is constant along the melting curve, it could allow for extrapolations to Earth's core conditions and the adiabatic heat flow to the top of the Earth's core to be estimated. The thermal conductivity will then be determined using the WFL using the Sommerfeld value of the Lorenz number. The value for the thermal conductivity will be used to calculate the total adiabatic heat flux to the top of the lunar OC. Along with estimates of heat flow through the CMB, these data will provide assessment of the likelihood of thermal convection in the Moon but may also be applied to other terrestrial bodies such as Ganymede, Mars and Mercury.

Chapter 2: Methods

2.1: Cubic anvil press

A 1000-ton cubic anvil press was used to pressurize an Fe10Ni wire sample to pressures ranging from 3-5 GPa. The wire sample was also heated while pressurized to temperatures up to 1970 K. The 1000-ton cubic anvil press achieved quasi-hydrostatic pressure on the wire sample by applying equal force synchronously to each face of the cube housing the wire sample. There are 6 anvils making up the 1000-ton cubic anvil press that advance in 3 directions perpendicular to each other. Each anvil is backed by a hydraulic ram (fixed to a steel frame) that moves the anvils together in the 3 perpendicular directions by coordinated movement that is constrained by the guide pins. The motion of the rams is regulated by oil pressure in a common pumping system. The anvils are composed of tungsten-carbide (WC) with 6 wt% cobalt (Co) used as a binding agent (Ito, 2007). An ohmic heating furnace was used to heat the sample up to temperatures above the melting point of the alloy after the pressure of the sample stabilized to the desired pressure. While the sample was heated to progressively higher temperatures, a DC test current was supplied to the sample and the DC voltage drop across the sample was measured to determine resistance. Figure 2.1 shows images of the 1000-ton cubic anvil press alone and the press with a computer, the Keysight B2961 power source, which provided the DC current, the Keysight 34470A multimeter that was used to measure the DC voltage, all set up for an experiment.

Figure 2.1a (left): An image of the 1000-ton cubic anvil press. Figure 2.1b (right): Experimental set-up: a DC current source and a multimeter are connected to the press, with a computer to read and display measured values.

2.2: Cell design one

Figure 2.2 is a cross section of the cubic cell design used to house the Fe10Ni sample. Table 2.1 gives the dimensions of the parts for each of the sections of the cube. The parts were machined to a tolerance of ± 0.002’’ to reduce leakage of the sample after it melted and to limit the movement of parts when force is first applied by the rams of the 1000-ton cubic anvil press.

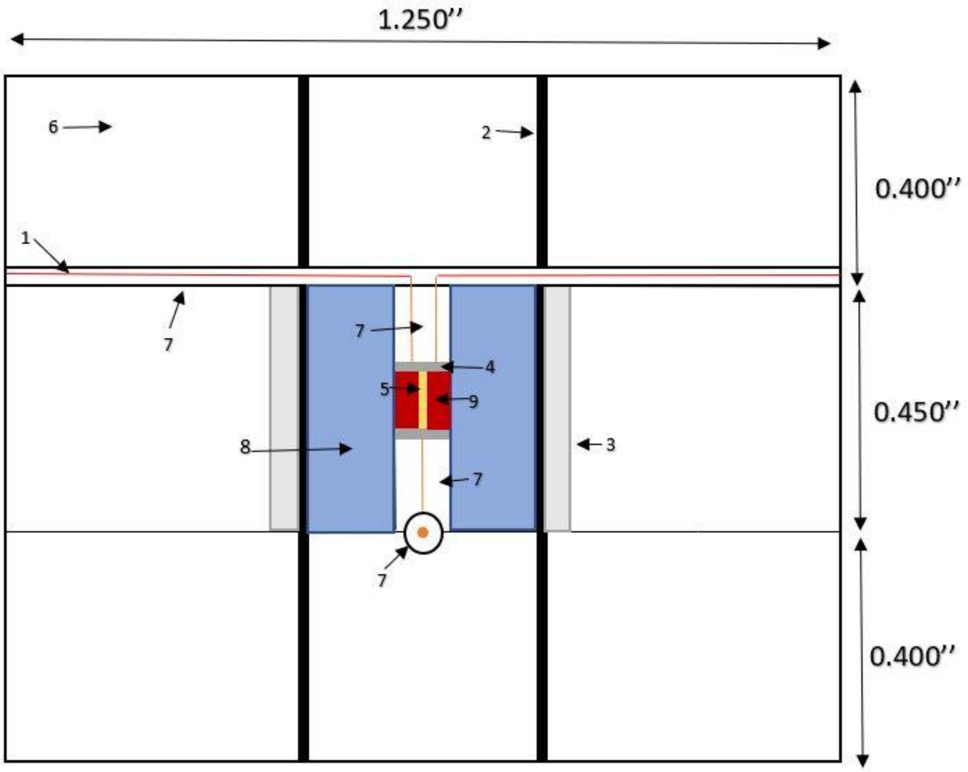

Legend

1: Type C thermocouples (TC)

2: Graphite furnace

3: ZrO_2 sleeve

4: Tungsten (W) disk

5: $Fe_{0.90}Ni_{0.10}$ wire sample

6: Pyrophyllite cubes

7: 4 – hole Al_2O_3 Ceramic tube

8: Boron nitride (BN)

9: Single hole Al_2O_3 ceramic tube

Figure 2.2: Cross section of the first cell design, with arrows displaying the locations of the various parts.

Table 2.1: Measured dimensions of the parts used to construct the cells that were used in the experiments.

Middle section (0.450’’x0.450’’. One 0.040’’ groove on each side to fit the TC)			
Part	***Inner diameter (ID) (±0.002’’)***	***Outer diameter (OD) (±0.002’’)***	***Length (±0.002’’)***
Zirconia sleeve	0.325’’	0.435’’	0.450’’
Graphite sleeve	0.270’’-0.280’’	0.320’’	0.450’’
Boron nitride sleeve	0.050’’	0.270’’-0.280’’	0.450’’
Tungsten discs	N/A	0.050’’	0.004’’
4-hole ceramic tube	N/A	0.050’’	0.120’’
Sample tube	0.015’’	0.050’’	0.070’’
Sample	N/A	0.015’’	0.070’’
Hafnium (surrounding TC in groove)	0.010’’	0.040’’	0.200’’
End sections (2) (0.400’’x0.400’’)			
Part	***ID (±0.002’’)***	***OD (±0.002’’)***	***Length (±0.002’’)***
Graphite sleeve	0.270’’	0.320’’	0.400’’
Pyrophyllite plugs	N/A	0.270’’	0.400’’

Most of the parts shown in the diagram were machined using a Sherline series 4400 lathe shown in figure 2.3, while some, such as the Hafnium were suppied by the Secco lab. The tungsten discs were cut by the machinist. The lathe was also used to sand, cut, and bore holes into the materials used.

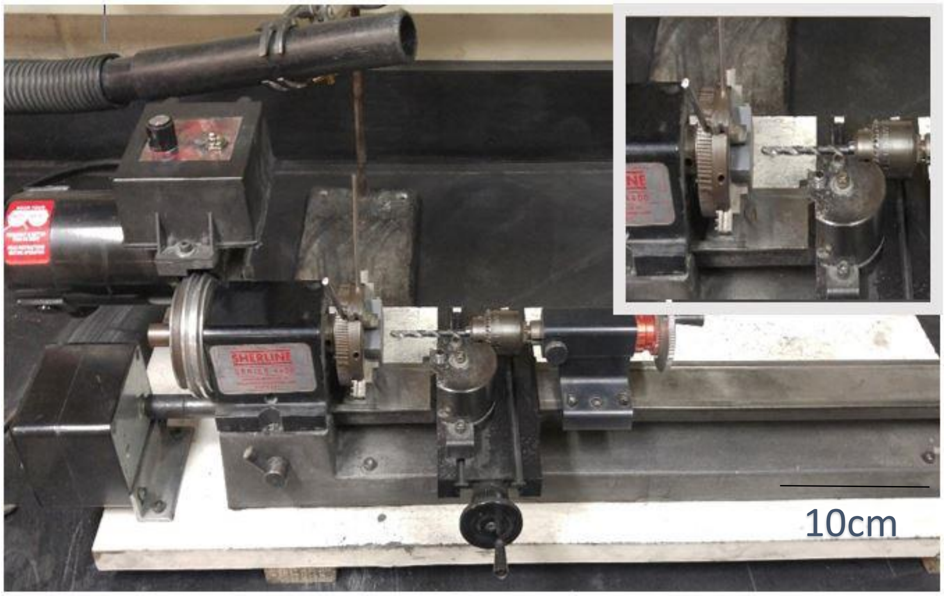

Figure 2.3: The Sherline series 4400 lathe shown was used to machine parts used to house the sample. Insert (top right): a middle section of the pyrophyllite cube is in a 4-jaw chuck with the drill set up.

2.3: Pressure transmitting medium

The sample was loaded into a pressure transmitting medium (the cube) before placement in the cubic anvil press. The medium used was the natural mineral pyrophyllite ($Al_2Si_4O_{10}(OH)_2$). Pyrophyllite was chosen because it has the following properties: 1) low internal friction to produce well-formed gaskets and to keep the sample in a quasi-hydrostatic state of stress. 2) very low thermal conductivity, which prevents internally generated heat from leaking out through the anvils. 3) very low electrical conductivity to provide electrical insulation within the cube to prevent wires and furnace components from short-circuiting. 4) a high melting point that increases with increasing pressure to maintain a solid pressure medium at high experimental run temperatures. 5) pyrophyllite is chemically inert and is stable at high pressures and temperatures. A large slab of pyrophyllite was machined into cubes with a side length of 1.250’’ using a milling machine. The cube was cut into 3 pieces, with the end sections measuring 1.250’’x0.400’’ and the middle section measuring 1.250’’x0.450’’. A 0.435’’ diameter hole was drilled into the middle section using the milling machine, and a 0.320’’ diameter hole was drilled in each of the end sections. The sample was placed in the hole in the middle section. 0.200’’ diameter holes were also drilled near the two diametrically opposing corners of each of the pyrophyllite cube sections. These holes were used for pyrophyllite pins which held the three parts aligned and firmly together. Figure 2.4 shows a set of four complete pyrophyllite cubes each with three sections.

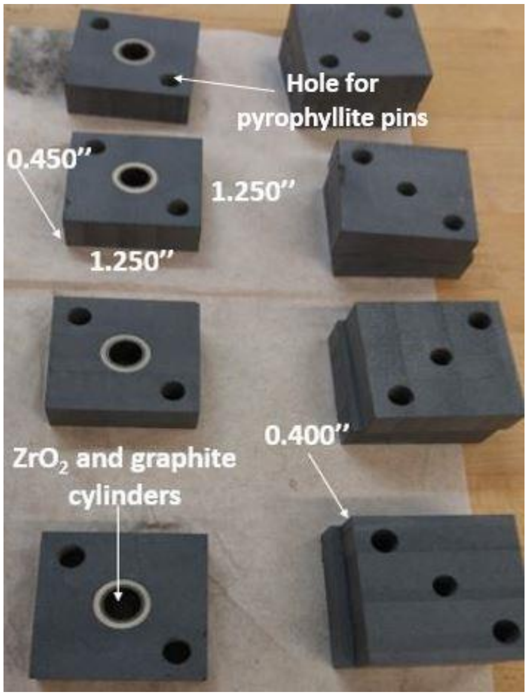

Figure 2.4: Sections of four complete cube assemblies. On the left, the middle sections of the pyrophyllite cubes are shown with the ZrO_2 *and graphite sleeves inserted in the centre hole. The end sections of the pyrophyllite cubes are on the right side of the image.*

2.4: Pyrophyllite plugs and pins

Cylindrical pyrophyllite plugs were machined using the lathe and placed in the end sections of the graphite furnaces to fill the furnace. Pyrophyllite pins measuring 1.250’’ in length with a diameter of 0.100’’ were placed into the holes drilled for the pins to hold the cube sections together.

2.5: Thermal insulating medium - ZrO_2

The zirconia (ZrO_2) sleeve was fabricated first by using a coring tool in a drill press to core a small cylinder from a rectangular slab of zirconia, giving the inner diameter of the zirconia cylinder. This inner diameter (ID) measured 0.320’’. The coring tool was then used to create a larger cylinder centered over the inner diameter. This produced an outer diameter (OD) of the hollow cylinder measuring 0.430’’. This outer diameter allowed the zirconia sleeve to tightly fit in the hole drilled in the middle section of the pyrophyllite cube. The zirconia was then modified to a length of 0.450 ± 0.002’’ using the Sherline series 4400 lathe so that the zirconia could fit in the middle section of the pyrophyllite cube snugly. To reduce heating of the zirconia, it was continuously flushed with water while machining. To remove water, oils from human contact, excess carbon on the surface from handling the graphite, and other impurities that may have contaminated the cylinder, the zirconia was placed in a furnace where it was heated to 750˚C for 50 minutes. The zirconia was used as the insulating medium for the sample because it is stable at high pressures and temperatures and is a good thermal insulator (Nielsen and Chang, 2005).

2.6: Graphite furnace

Graphite was used as a resistive heating furnace by using a 350V voltage source to generate an AC current of 2.00 A that was passed through the graphite to heat the sample through ohmic heating. Graphite worked well as the heating furnace because it is an intermediate conductor, not as conductive as a metal but still conductive, so there is still a large amount of electron scattering. This scattering causes the motion of the electrons to become random, constituting thermal energy. Graphite was machined using the lathe to form a cylinder 0.450'' in length for the middle section of the cube and 0.400'' in length for the top and bottom sections of the cube. The furnace for the middle section was machined to have a wall thickness of 0.040'' ± 0.002'' while the end sections were machined to have a wall thickness of 0.050'' ± 0.002''. The end sections were machined to be slightly thicker in case parts shifted while the cube was being pressurized. This allowed for overlap of the furnaces even if parts shifted, so heating could still occur. A thicker furnace provided slower heating but was easier to machine and less fragile. The thinner graphite furnace in the middle section also ensured that the greatest heating would be in the central section where the sample is located. The graphite cylinder was then placed inside the zirconia cylinder. This cylinder is shown in figure 2.5.

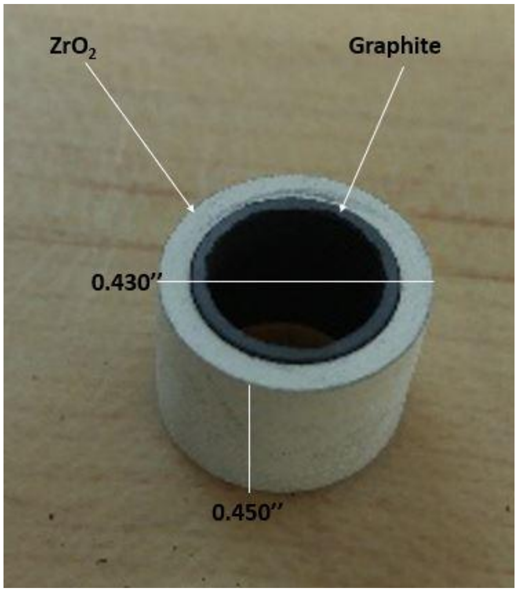

Figure 2.5: After the zirconia was heated in the furnace to clean it, the graphite furnace was placed inside. This part was placed in the middle section of the pyrophyllite cube.

2.7: Confining medium around the sample

The confining medium used to house the sample was machined from a cylinder of Boron Nitride (BN). The machined cylinder had a length of 0.450'', an ID of 0.050'' and an OD of 0.270''-0.280''. This cylinder was placed inside the graphite sleeve. The zirconia cylinder containing the BN and the graphite cylinders was then placed in the hole of the middle section of the pyrophyllite cube. A groove 0.040'' in diameter was then machined into the top and bottom of the middle section of the pyrophyllite cube after the cylinders were placed inside the hole. Figure 2.6 shows the middle section after this step. The thermocouples (TCs) would be placed in this groove. BN was used as the confining medium between the furnace and the sample because it is soft, has a relatively high melting temperature, is chemically inert, has a high electrical resistivity, and provides a quasi-hydrostatic environment (Greim and Schwetz, 2005).

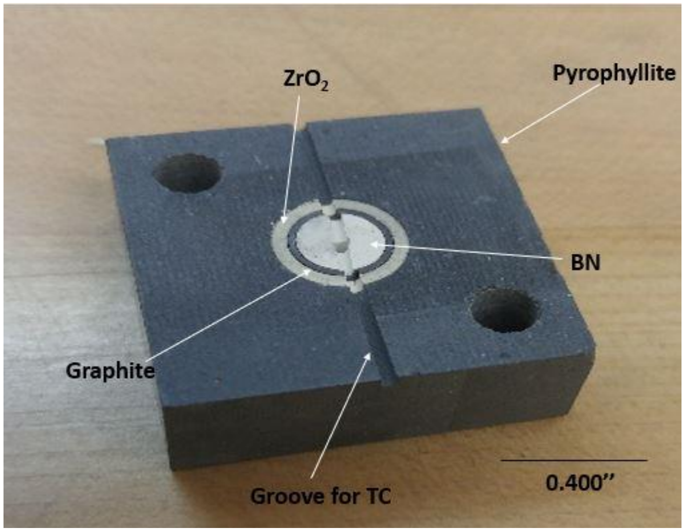

Figure 2.6: A middle section of the pyrophyllite cube after the zirconia, graphite, and BN cylinders are all placed inside the hole. The centre groove was cut by the machinist and was where the TC wires were placed.

2.8: Sample jacket and sample

An Al_2O_3 single hole ceramic tube was used as the sample jacket for the Fe10Ni wire sample. The single hole ceramic tube was cut using a zip wheel from a longer piece to 0.070'' in length and had a pre-cut ID of 0.015'' and an OD of 0.050''. The Al_2O_3 tube was chosen because of its low reactivity with iron alloys and low electrical conductivity. The low reactivity ensured that aluminium or oxygen did not leech into the sample during pressurization and heating, keeping the sample pure. The low electrical conductivity ensured the voltage was not passed through the ceramic tube, so the measurement of the voltage drop was only across the sample.

The Fe10Ni wire sample was cut from a 0.015'' diameter wire of $Fe_{0.90}Ni_{0.10}$ that was custom-manufactured by Chem Pur – EUR (Germany). The wire was cut and sanded down to a length of 0.075'' using a zip wheel and then cleaned in an ethanol bath before assembly of the middle cube section. Cleaning in an ethanol bath ensured oils from being handled were removed from the sample.

2.9: Tungsten disks

Tungsten (W) discs were used to improve the contact between the electrodes/thermocouples and the sample. The W disks were 0.004'' thick with a diameter of 0.050''. W was chosen because it is a good electrical conductor and does not react with Fe-Ni although diffusion of W into the sample is a concern especially in the liquid state. Because of the low electrical resistivity of W and because of how thin the disks are, they constitute a negligible contribution to the voltage drop between the two ends of the sample.

2.10: Thermocouples

A Type C Tungsten/Rhenium (95%W/5%Re – 74%W/26%Re by weight percent) alloy thermocouple (TC) was used to measure the temperature of the sample. The thermocouple also functioned as electrodes and could measure the voltage drop across the sample. This type of TC was chosen because they will function up to 2329˚C, which is well above the temperatures necessary to melt the Fe-Ni alloy (Pollack, 1991). Thermocouple wires for each leg was threaded through a 4-hole Al_2O_3 ceramic tube that was cut to a length of 0.120''. The legs were crossed over each other at one end, forming a junction that would be pressed together during the experiment. One TC was placed at each end of the sample, with the TC junction in contact with the W disc. The TCs measured the temperature at each end of the sample. This helped to determine when measurements needed to be recorded, when the sample was melted so the AC current flowing through the graphite furnace could be stopped, and if any temperature gradients were present in the sample during heating. The TCs also served the function of electrodes to measure the voltage drop across the sample.

2.11: Cell assembly

To assemble the cell, the middle section of the cube was placed on a brass stand, with a small portion of the stand fitting inside of the BN hole to keep the parts placed in the BN hole level. A W disc was placed in the BN hole, followed by the single hole ceramic tube that housed the sample. Another W disc was placed in the hole, sitting on top of the sample. A TC was placed in the BN hole and cemented in place. The middle section was then turned over and the TC was placed in the other side of the hole and cemented in place. The TCs were then cemented in the hole in the BN. The ends of the TC wire were inserted into a Hafnium (Hf) tube to reduce unwanted contact and to limit movement of the TCs during pressurization. The Hf tubes containing the TC wires were placed in the grooves leading to the outside of the cube. The middle section was then placed between the top and bottom sections of the pyrophyllite cube. Two small, square pieces of copper (Cu) foil were cut from a larger sheet, and a small hole was punctured into the center of the foil. The TC wire sticking outside the cube was threaded through the Cu foil and wrapped around it. This increased the electrical contact between the TCs and the anvils. The pins were then inserted into the pin holes to hold the sections together. The cube was painted with iron oxide to enhance friction at the cube-anvil interface which promotes formation of the gaskets. Figure 2.7 is an image of a finished cube that shows the location of the pyrophyllite pins, pyrophyllite plugs, copper foil and graphite furnace.

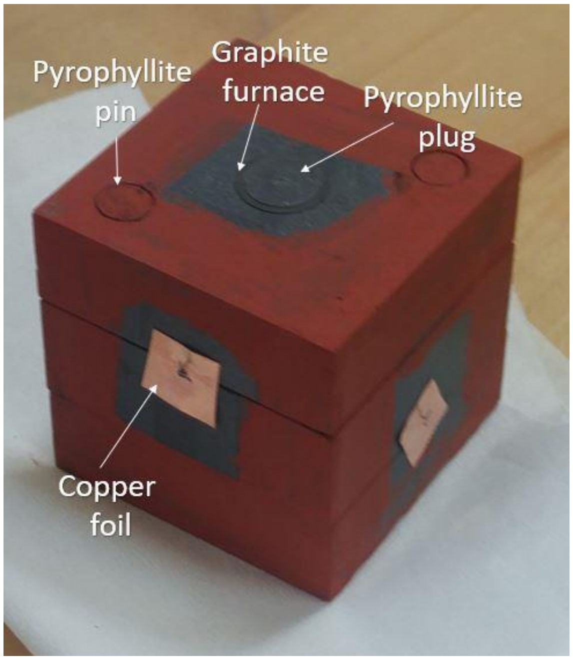

Figure 2.7: A prepared cube (1.250'' edge length) before an experiment is conducted.

2.12: Cell design two

Several small alterations to the previous cell design were used after four experiments to better contain the pyrophyllite plugs and improve the contact between the TCs and the W disk. A cross section of this cell design is shown in figure 2.8. Zirconia disks that were 0.050'' thick and 0.275'' in diameter were placed in the end sections of the cell, between the pyrophyllite plug and the middle section of the cell. They were used to improve the thermal insulation of the cell and to better contain the sample in the sample jacket and the pyrophyllite in the graphite furnace. The zirconia disk in the end section is shown in figure 2.9. Grooves were made in the TCs to improve the contact between the TCs and the W disk.

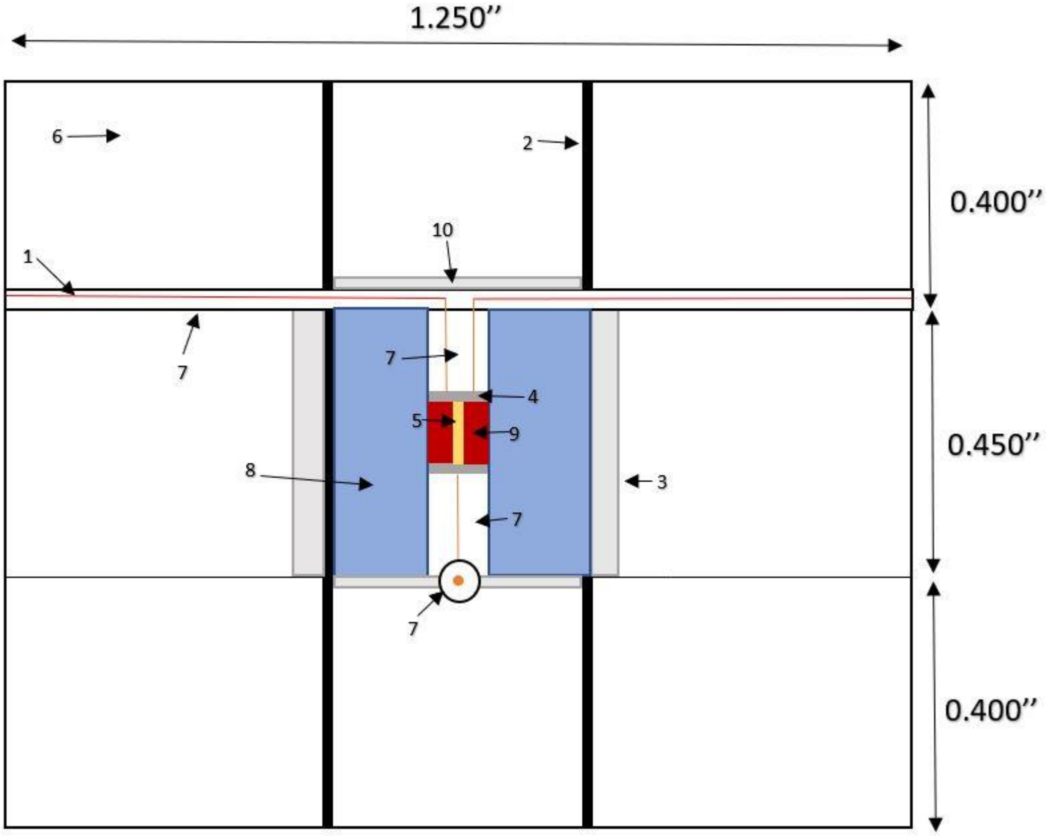

Legend

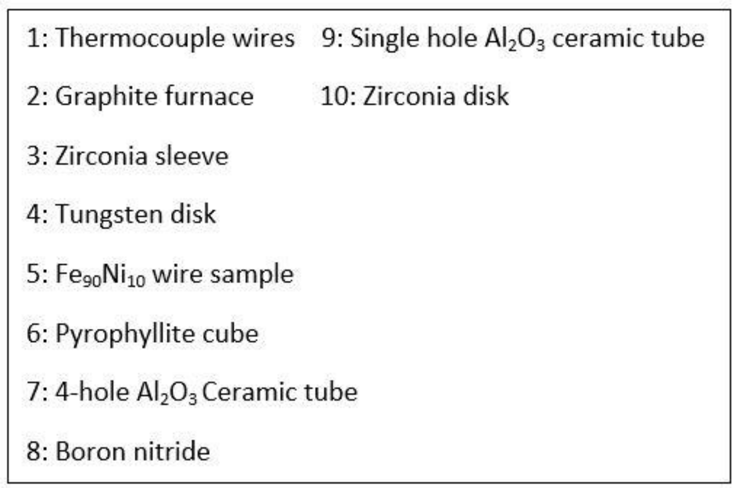
1: Thermocouple wires
2: Graphite furnace
3: Zirconia sleeve
4: Tungsten disk
5: $Fe_{90}Ni_{10}$ wire sample
6: Pyrophyllite cube
7: 4-hole Al_2O_3 Ceramic tube
8: Boron nitride
9: Single hole Al_2O_3 ceramic tube
10: Zirconia disk

Figure 2.8: The second cell design. Changes from previous design was the inclusion of zirconia caps to better contain the sample, pyrophyllite plugs, and provide better insulation. The grooves in the 4-hole ceramic tube were to improve the contact between the TCs and the W disks.

Figure 2.9: end section of the cell with the zirconia disk to improve containment.

2.13: Electrical resistivity and resistance

In the experiments, a voltage mode switch was used to alternate between measuring the voltage drop across the sample and the temperature of the sample. The temperature of the sample was measured by the thermal electromotive force (emf) generated by the individual TC's. An excel program was used to convert the thermal emf to absolute temperature. When used as electrodes, the voltage drop could then be used to calculate the electrical resistance, given by Ohm's law:

$$R = \frac{V}{I} \tag{6}$$

where R is the electrical resistance of the sample, V is the voltage drop across the sample, and I is the electrical current that was passed through the sample. The electrical resistivity of the sample was then calculated by using Pouillet's law:

$$\rho = \frac{RA}{l} \tag{7}$$

where ρ is the electrical resistivity and A is the cross-sectional area of the cylindrical sample.

2.14: Analysis of recovered sample

After the experiment was performed, the cube was removed from the cubic anvil press. Figure 2.10a shows the recovered cube with the gaskets still attached. Figure 2.10b shows a cube before and after an experiment was conducted. The recovered cube was then broken open and the BN housing the sample was removed, along with its contents. It was glued to a small plastic slide using epoxy. Once the epoxy dried, the BN housing was sanded down until the sample was visible. A Buehler EcoMet 30 single grinder was used to further grind the sample down until the largest measured diameter of the sample was reached. Measurements of the recovered sample at its maximum diameter could then be used in the calculation of the electrical resistivity from the voltage drop values. Images were also taken using the Nikon SMZ800 microscope under 3-5X magnification to measure the geometry of the sample and to see if any contamination of the sample was visible. The measured geometries were used in calculations of the electrical resistivity.

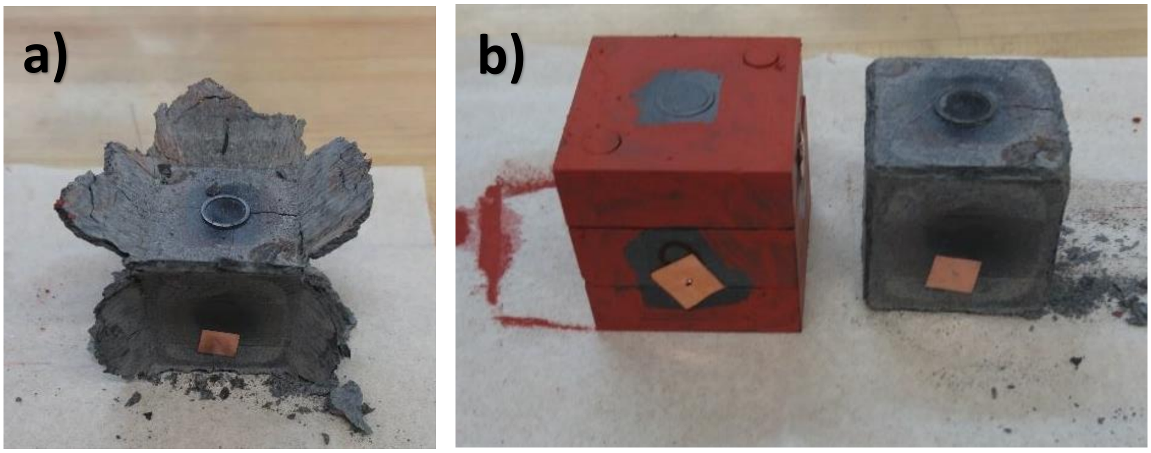

Figure 2.10a (left): A recovered cube after an experiment. The gaskets are still attached to the cube but are very fragile. Figure 2.10b (right): A comparison between a recovered cube (1.25'' edge length) and a cube before an experiment is conducted. The recovered cube is noticably smaller. The size reduction is mainly due to removal of the pyrophyllite that flowed between the anvils while the cube was pressurized, which formed the gaskets shown in figure 2.10a, rather than compression of the cube.

2.15: Electron microprobe analysis

Electron microprobe analysis (EMPA) was conducted in the Earth and Planetary Materials Analysis Laboratory on three of the samples recovered from the experiments. EMPA uses a beam of focussed electrons that are used to excite x-rays from a small region of the specimen. The x-ray wavelength is measured by x-ray spectrometers. Since each element emits a characteristic spectrum, the elements and the concentration of the elements can be identified from the region (Reed, 2005). The EMPA was conducted on metallic regions of the sample and the boundaries of the sample to determine if any diffusion occurred across the boundaries and that the sample was still pure. A thin coating of graphite was applied to the samples prior to being placed in the JEOL JXA-8530F electron microprobe to avoid charging effects on the sample surface. The samples were bombarded with a 20 KeV electron beam voltage with a 50 nA probe current to analyze 1μm^2 areas of the sample.

Chapter 3: Results and discussion

Experiments using the first cell design

3.1: Experiment 1

Cell design 1 was used to conduct four experiments in the 1000-ton cubic anvil press. For experiment 1 (Exp 1), the voltage drop across the sample was measured after the sample was pressurized to 4 GPa and then was progressively heated until reaching temperatures slightly above the melting point of the Fe-Ni alloy. Figure 3.1 is a phase diagram of Fe-Ni alloys and was used to approximate the melting temperature at high pressure and to guide the choice of highest T in the experiment.

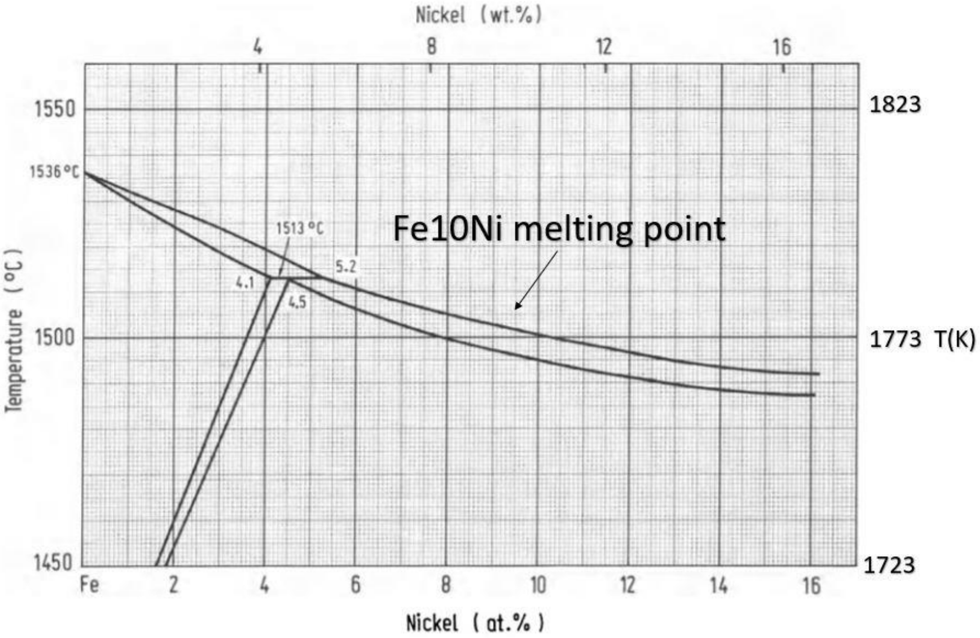

Figure 3.1: Phase diagram of the Fe-Ni binary alloy system at 1 atm (Kubaschewski, 1982).

During pre-heating, which is done to ensure good electrical contact between the TCs and the sample, the voltage drop across the sample sharply increased at 1050 K. The T was lowered to room T and the sample was then heated to 1973 K, far above the melting point of the alloy, to attempt to regain electrical contact. Because of this, the data above 1050 K is unreliable. Figure 3.2 is an image of the recovered sample from Exp 1 taken using the Nikon SMZ800 microscope after the sample was ground down to the halfway point using the Buehler EcoMet 30 single grinder. The halfway point was the depth where the maximum width of the sample was measured. This was used in the calculation of the electrical resistivity. Figure 3.2

shows the Fe-Ni alloy sample was well contained in the ceramic sample tube melting, which can be an issue, since the melt can escape the sample tube.

Figure 3.3 is an electron backscatter image (EBS) of the sample taken during EMPA analyses. In total, 49 locations were probed. The detailed EMPA results, which are included in the Appendix, showed that the sample had a large amount of W diffusion. This occurred when the Fe-Ni sample was melted. In the melt phase, the sample was highly reactive with the W, causing a W, Fe, Ni alloy to form. The probe showed that there was on average 49 wt% Fe, 44 wt% W and 6 wt% Ni in the ceramic sample tube after the experiment was conducted. When there is a large amount of W diffused into the sample after melting such as this, it is an indication that the sample was heated to a temperature too far above the melting point of the Fe-Ni alloy. The melting point of Fe10Ni is around 1780 K at 1 atm (Kubaschewski, 1982). In order to account for the increase in melting temperature with increasing pressure, 30-40 K was added to the melting temperature for each 1 GPa of additional pressure. The aim was to heat to 1920 K to ensure melting, since the exact melting point is not known, but to limit W diffusion into the sample. In future experiments, the sample was heated to lower temperatures than Exp 1.

Along with W diffusion in the sample impacting the electrical resistivity, there was also BN infiltration into the sample. Figure 3.3 shows the BN infiltration at the top of one end of the sample. The infiltration could have occurred because a W disk was bent slightly upwards during assembly or subsequent pressurization, allowing the BN to enter the top of the sample region. Because BN has very high electrical resistivity, the voltage drop across the sample sharply increased once it started entering the sample tube. This problem was fixed in future experiments by altering the method of inserting the sample and W disks during assembly of the cell.

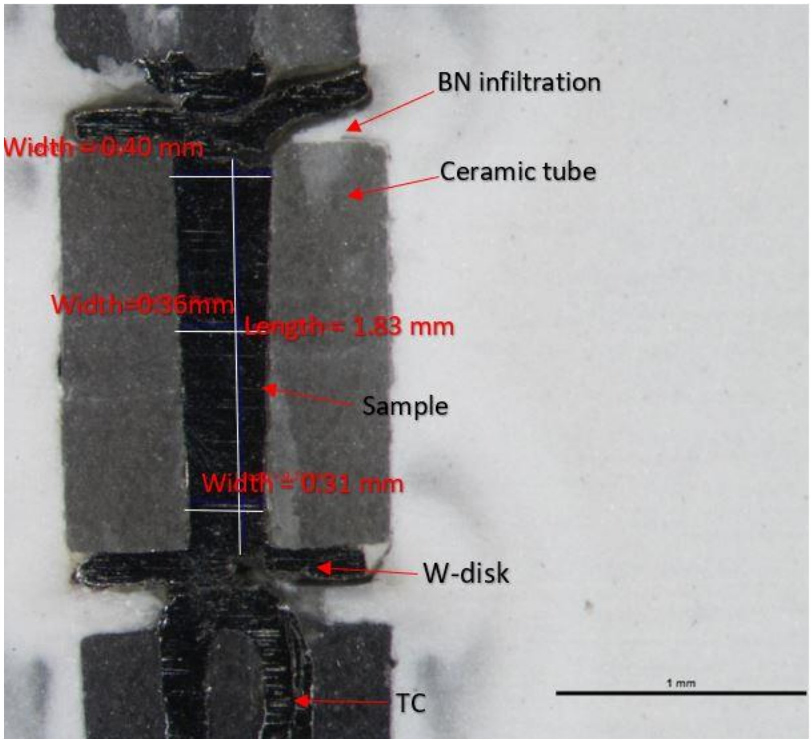

Figure 3.2: Recovered experiment 1 sample (4GPa, 1973K) after grinding to determine geometry. The W disk is bent, allowing BN to infiltrate into the sample tube.

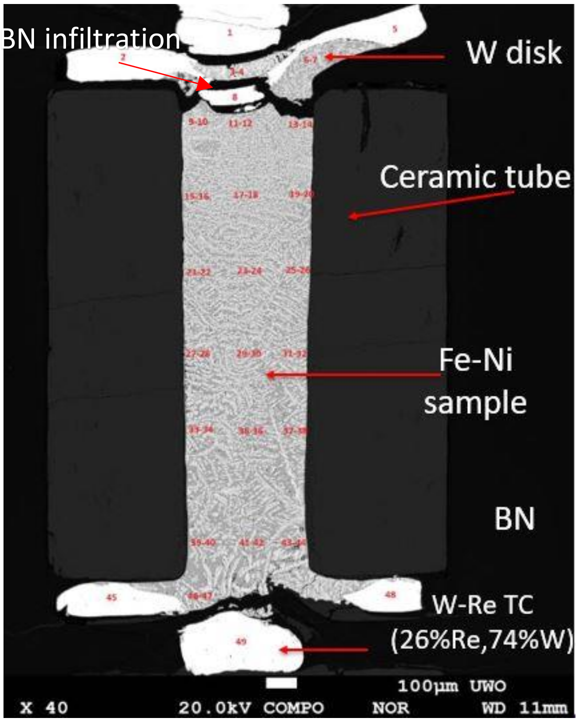

Figure 3.3: EMPA conducted on Exp 1. The numbers indicate locations where the composition was probed using the EMPA. Pervasive W diffusion is visible in the sample, with the white being the diffused W and grey being the Fe-Ni alloy.

3.2: Experiment 2

Exp 2 was conducted at 4 GPa again since the last data set was unreliable above 1050 K. Electrical contact between the TCs and sample was maintained the entire time during this experiment. There was no sharp voltage drop increase like the prior experiment until the sample was above the melting temperature of the alloy. The sample was heated to 1920K, at which point the voltage drop increased slightly, indicating the sample had melted. After several seconds in the melt, the voltage drop started to sharply increase, indicating electrical contact was lost or another material infiltrated the sample tube. Figure 3.4 is the cross section of sample 2 recovered from Exp 2 after the sample was ground down to the depth of maximum length and width. A large portion of the sample appears to have leaked out of the ceramic tube during the melt phase, with pyrophyllite having entered the single hole ceramic tube and replaced most of the sample, leaving 0.21 mm of sample left at one end of the sample tube. To determine that it was pyrophyllite that replaced the sample in the ceramic tube after the sample melted, EMPA was conducted on the sample and surrounding areas. Using the Energy Dispersive Spectrometer (EDS), the composition of the material in the ceramic tube was confirmed to be pyrophyllite. The remaining sample reacted with the W disk when the sample reached the melt phase, forming a mixture of W, Ni and Fe. Figure 3.5 shows images of the remaining sample taken during the EMPA. Figure 3.6 shows a possible path the pyrophyllite took to enter the sample tube. The pyrophyllite appears to have travelled down the remaining space in the hole of the 4-hole ceramic tube that housed the TC legs. This allowed the pyrophyllite to reach the area where the sample is housed. The source of the pyrophyllite could have been from the pyrophyllite plugs. To fix the issue of the pyrophyllite migrating into the sample tube, zirconia disks were used in the experiments after Exp 4 between the pyrophyllite plugs and the TCs in the end sections. The added zirconia disks would also improve the efficiency of heating the sample.

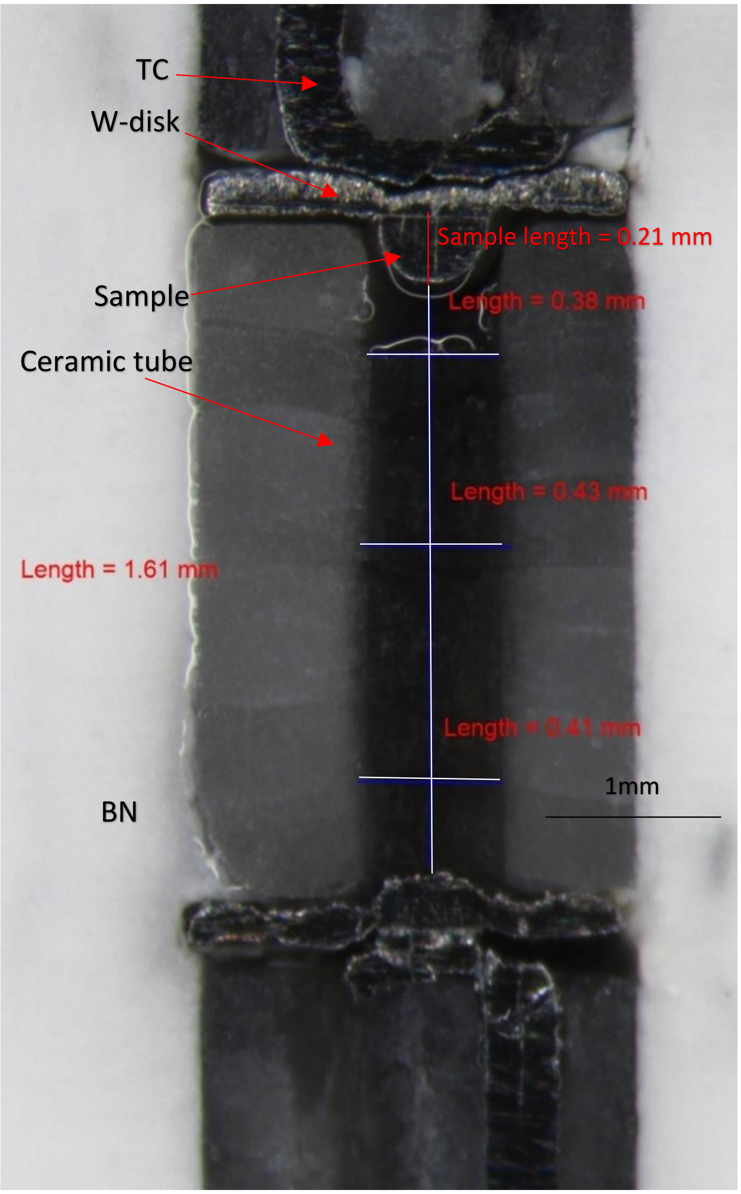

Figure 3.4: Recovered Exp 2 sample (4 GPa, 1920 K) after the sample was ground to the point where the maximum width was measured. The length measured is the length of the sample that was replaced by pyrophyllite. 0.21mm is the remaining sample size and this length is shown using the red line. The length of the pyrophyllite and the sample added together, along with an average of the widths, was used to calculate the electrical resistivity.

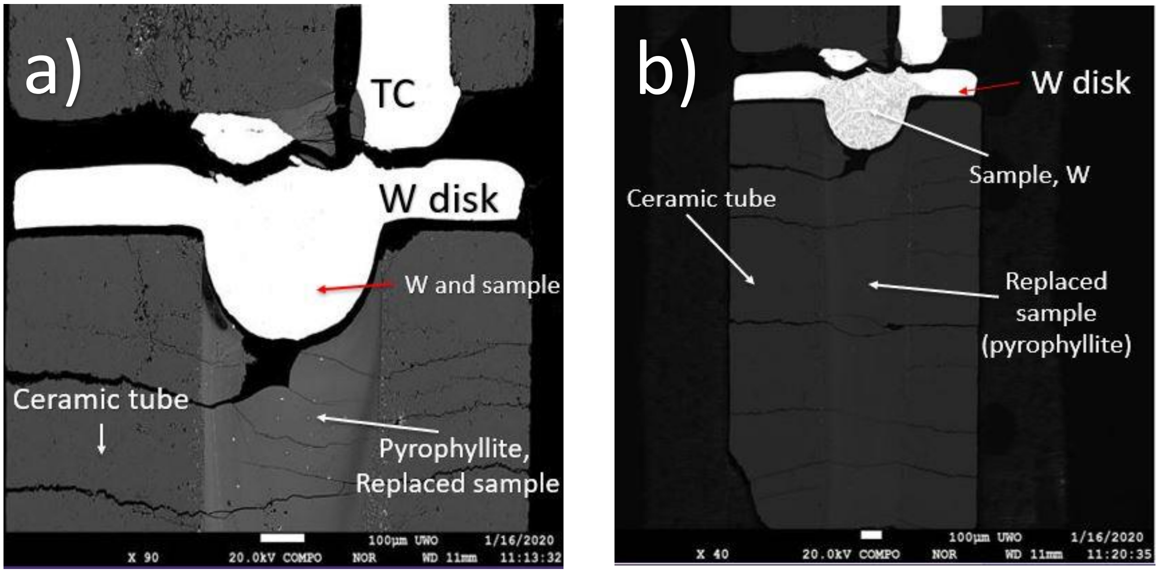

Figure 3.5a: Image of the remaining portion of the Fe-Ni sample. b: A larger scale image of the remaining sample. W diffusion into the Fe-Ni sample can be seen in this figure. The grey is the Fe-Ni alloy and white is W. This diffusion occurred once the sample had melted.

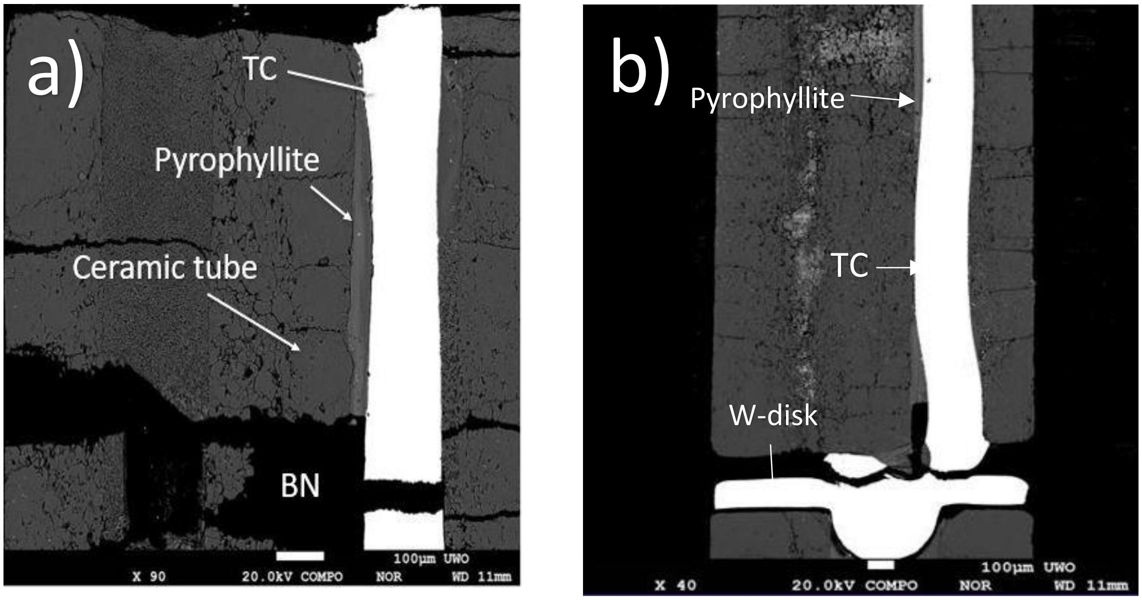

Figure 3.6a: Pyrophyllite is shown next to the TC, indicating this could be a path the pyrophyllite took. b: The pyrophyllite is shown travelling along the TC down to the W-disk.

3.3: Experiment 3

Figure 3.7 shows the cross section of the sample recovered from Exp 3 after the sample was ground. Exp 3 was conducted at 3 GPa. The sample appears to have leaked out after melting to be replaced with pyrophyllite as occurred in Exp 2. The entire sample leaked out and there is no Fe-Ni alloy remaining in the sample tube. Figure 3.8 is an image taken before EMPA was used to probe the remaining composition. The path of the pyrophyllite to reach the sample tube was likely through the 4-hole ceramic tube, since this was likely the pathway for pyrophyllite for Exp 2. This sample was heated twice, once to 1350 K, and was immediately quenched once the voltage drop across the sample showed a sharp increase. The voltage drop stayed very high after quenching. The sample was then heated a second time to 1800 K to see if the voltage drop would decrease with heating, but it did not. Because of this, the data above 1350 K is unreliable.

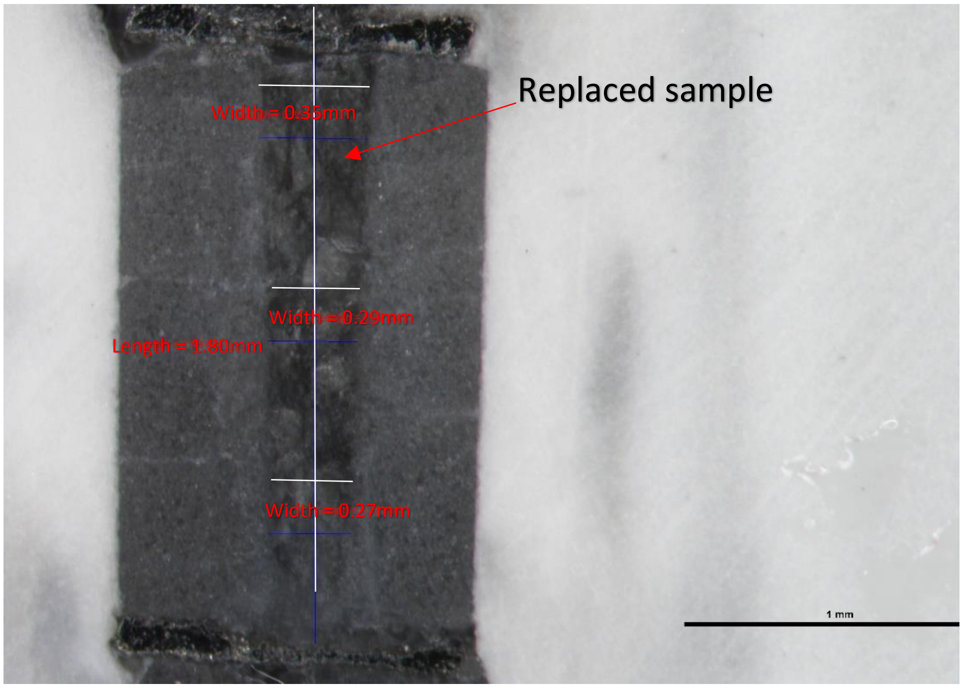

Figure 3.7: Recovered Exp 3 sample (3 GPa, 1930 K) after being ground to the midway point to determine geometry. The sample was fully replaced by pyrophyllite.

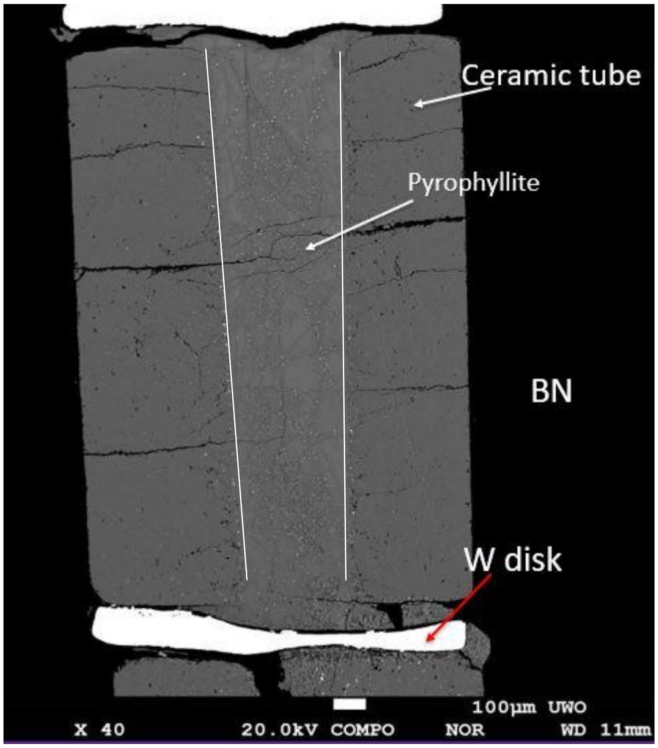

Figure 3.8: Image taken during EMPA of sample 3. The sample leaked out of the cell during heating and was replaced by pyrophyllite.

3.4: Experiment 4

Exp 4 was conducted at 3 GPa. Figure 3.9 is an image of the ground down cross section. Sample 4 was lost while the sample was being polished, so the sample was not probed using EMPA. During the experiment, the sample was pre-heated, then heated to 1200 K, at which point the voltage drop across the sample sharply increased, meaning contact was lost or there was infiltration into the sample tube and the TCs. As a result, the data are unreliable above 1200 K. The sample was heated until 1720 K, at which point the current was turned off and the sample was cooled. As with Exp 2 and Exp 3, pyrophyllite entered the sample tube, possibly through the 4-hole TCs was shown to be the likely pathway in Exp 2. The image shows that the sample was not fully replaced by pyrophyllite. The ceramic tube also changed colour in the area where the pyrophyllite was, indicating it may have reacted with the sample tube. A reason the solid Fe10Ni wire sample may have been replaced by pyrophyllite in these experiments is due to extra space in the sample tube the sample sits in. These are pre-made parts and could not be altered, and there was a size difference in the OD of the Fe10Ni wire sample and the ID of the sample tube. Pyrophyllite could have been forced into the tube along with the sample during compression. The pyrophyllite plug could have been heated by the graphite furnace of the end sections, causing melting and allowing it to easily flow in the cell downwards towards the sample before the sample melted. The TCs may have then started measuring the voltage drop of some pyrophyllite, causing it to increase sharply. The release of water of hydration in the pyrophyllite on heating (Hicks and Secco, 1997) could also cause a decrease in the melting temperature of the sample if the pyrophyllite and sample came into contact, allowing the sample melt to escape due to insufficient containment and allowing pyrophyllite to flow into the sample tube to replace it.

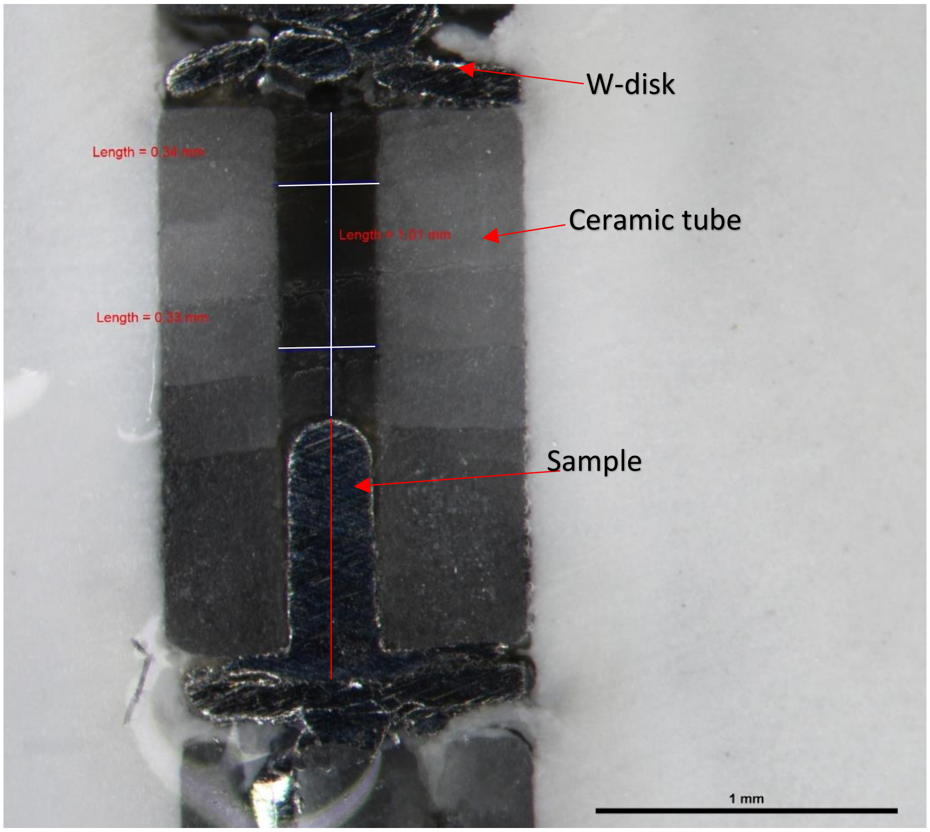

Figure 3.9: Recovered experiment 4 sample (3 GPa, 1720 K) after grinding to the midway point to determine geometry. The remaining sample is visible in the figure, with the length of remaining sample shown in red, along with the pyrophyllite that infiltrated the single hole ceramic tube.

Experiments using the cell design two

3.5: Experiment 5

Cell design 2 utilized zirconia disks to increase containment of the sample, the pyrophyllite plugs, and to increase the efficiency of heating. Exp 5 and Exp 6 used this design change. Exp 5 did not gain any contact with the anvils and no current could be driven through the graphite furnaces. This could be due to a small space between the TC and the W-disk on one side of the sample, as shown in the cross section in Figure 3.10. This would create an incomplete circuit, and no measurements could be made by the TCs as a result. The cause of this small space could be because of a fit too tight between the 4-hole ceramic tube and the sample tube, stopping the TC from moving all the way down the sample tube to reach the W-disk while the cell was being assembled. Because of this, Exp 5 was pressurized to 5 GPa and was only heated to 400 K. The purpose of the experiment was modified to simply check geometry and probe starting composition of the Fe10Ni wire sample following pressurization only. Nine points on the sample were chosen and the composition of these points was determined using EMPA. An image of the points chosen is shown in Figure 3.11. The EMPA data (see Appendix) show the sample was nearly exactly Fe10Ni, which indicated the starting sample used in all experiments was the purity required.

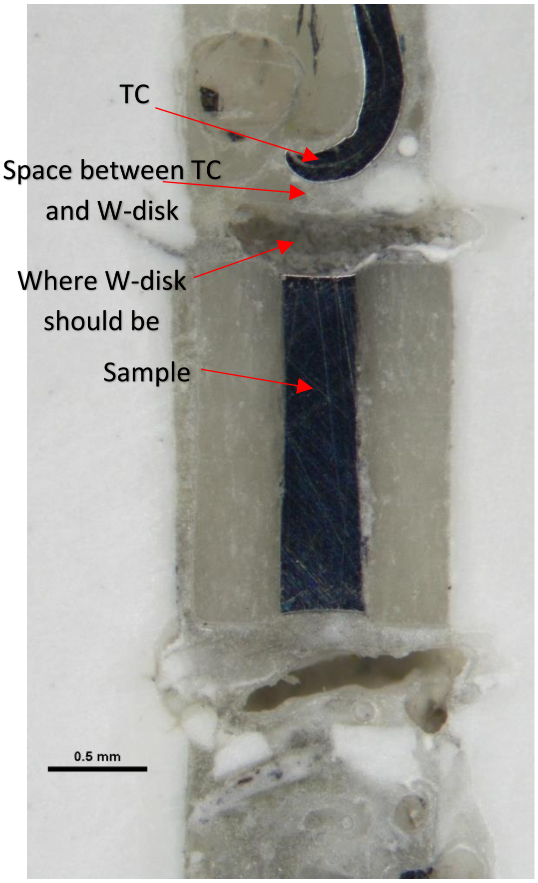

Figure 3.10: Recovered sample from Exp 5 (5 GPa, 400K) after the sample was ground down. The sample was heated only to 400K and as a result, the W-disks and parts of the TCs fell out while the sample was ground. The contact issue with this experiment could be due to a small space between the W-disk and TC on one end.

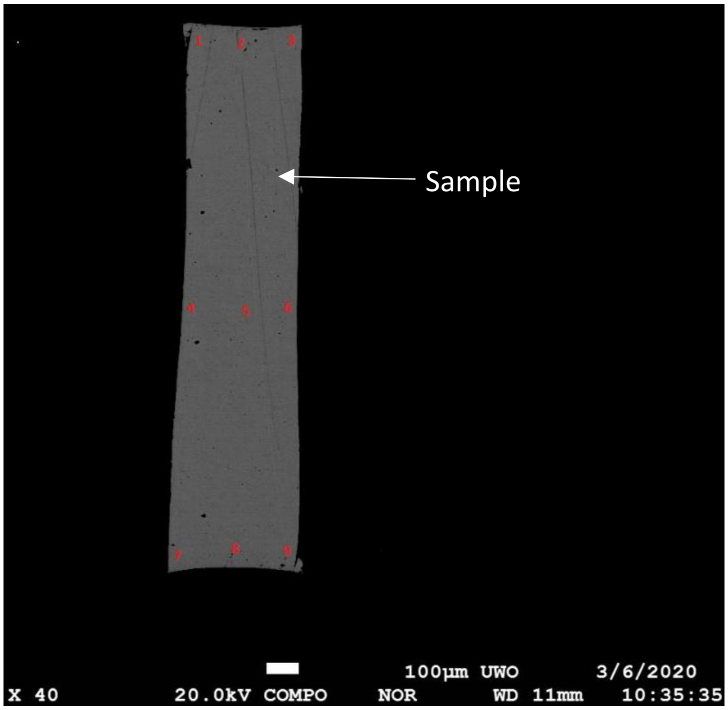

Figure 3.11: EMPA image of recovered sample 5. The red numbers are the points where the sample was probed. This probed data was used to confirm the purity of the starting composition of the Fe-Ni alloy used in the experiments.

3.6: Experiment 6

Exp 6 was pressurized to 5 GPa and heated to 1150 K, at which point the voltage drop across the sample sharply increased, indicating that contact was lost between the sample and TCs or another material infiltrated the sample tube. The sample was heated until 1684K, which is before the alloy should approach the melting point. Due to BN infiltration into the sample tube, the melting temperature of the alloy was lowered below the theoretical temperature and the sample melted. The EMPA data show that the recovered sample is approximately 70wt% Fe, 8wt% Ni and 21wt% W. Figure 3.12 is the image of the recovered sample after being ground down and Figure 3.13 is the image of the points that were probed during EMPA. There is BN infiltration into the sample tube on one side, which would cause an increase in the voltage dropped measured across the sample. This infiltration could be due to shifting of the Fe10Ni wire sample during assembly due to imperfect fit in the sample tube. The wire was more exposed on one side of the sample tube than the other, pushing the W disk down and away from contact with the sample tube and providing space for the BN to infiltrate the sample tube during pressurization.

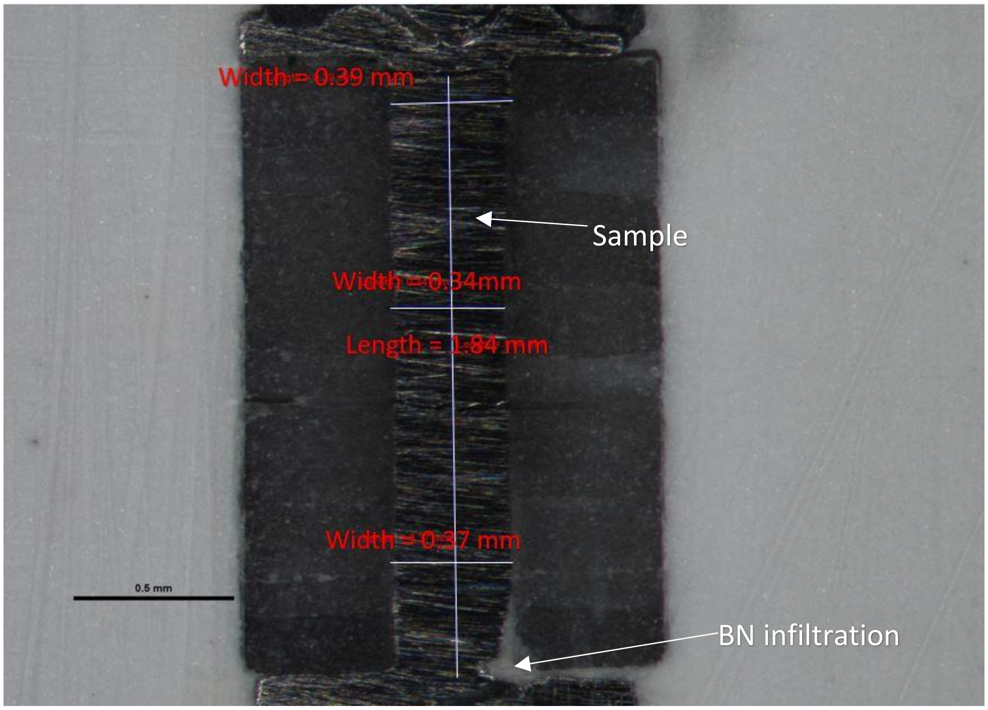

Figure 3.12: Cross section of the recovered sample from Exp 6 (5 GPa, 1684 K) after it was ground down. The sample was not melted unlike in previous experiments so that W diffusion before sample melting could be determined.

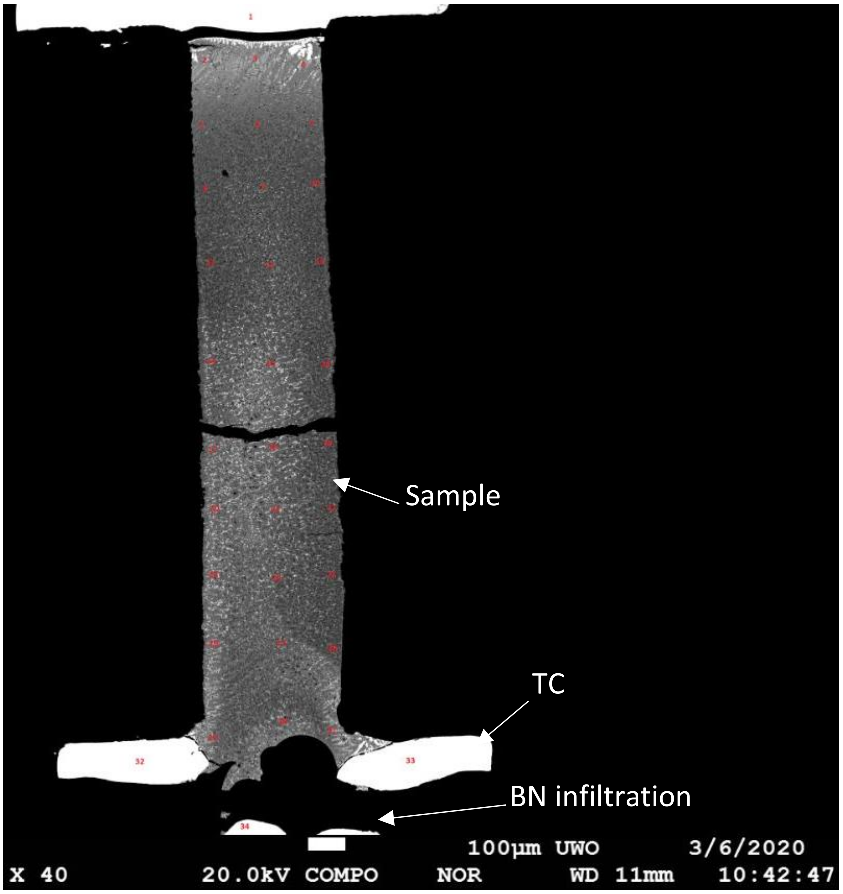

Figure 3.13: EMPA conducted on sample 6. The red numbers are the probed points. The probe image shows pervasive BN infiltration into the sample tube decreasing the melting point of the sample and causing the sample to melt before it's theoretical melting point.

3.7: Electrical resistivity

The data collected from Exp 2, 3, 4 and 6 are plotted together in Figure 3.14. The data show that the electrical resistivity increases according to the T^2 temperature dependence in the low T ferromagnetic state prior to reaching the Curie temperature (T_c) (Campbell and Fert, 1982). This behaviour terminates at around 850 K, which is the T_c of the Fe10Ni alloy. Above the T_c, the magnetic moments that are caused by the spin of electrons become randomly aligned in paramagnets and the material loses its ferromagnetic properties. Scattering due to spin disorder is at a maximum at T_c, which is responsible for the sharp increase in electrical resistivity. The T_c at 1 atm for pure Fe is 1040 K, whereas for Ni it is 631K, so the effect of alloying with Ni resulted in a lower T_c than pure Fe for the alloy. At a T above T_c, the contribution to the electrical resistivity due to spin disorder of the magnetic moments becomes constant (Drchal et al., 2017; Ezenwa and Secco, 2019). Following this jump, the electrical resistivity increases nearly linearly, with a smaller increase with temperature than before the T_c. This could be due to a relative reduction in electron – magnon scattering due to increased phonon – electron scattering at increasing temperatures and by the long-range order of spin magnetic moments. Exp 3, 4 and 6 then lose electrical contact between 1150 K and 1400 K. The electrical resistivity of Exp 2 continues to increase until the melting point of the Fe-Ni alloy is reached at around 1800 K. the sample is not fully melted until about 1850 K due to a phase loop in the phase diagram of the alloy (Figure 3.1). The electrical resistivity of the melt phase was 150 μΩcm at 4 GPa for the Fe10Ni alloy. This constitutes about a 10-15% increase in the electrical resistivity from the solid phase to the liquid phase, consistent with previous multi anvil press experiments on pure Fe (Secco and Schloessin, 1989). The electrical resistivity of pure Ni measured by Silber et al., (2017) appears to show about a 50% increase upon melting, significantly larger than that of pure Fe measured by Secco and Schloessin (1989) and Silber et al (2018). The increase in electrical resistivity on melting for the Fe10Ni alloy at room temperature was measured by Ho et al., (1983) to be about 5%. This is smaller than the previous measurements on pure Fe and pure Ni and in disagreement with the data collected in this thesis. Further study of the increase in the electrical resistivity above the melting point is needed to quantify the effect increasing pressure has on the electrical resistivity during and after melting.

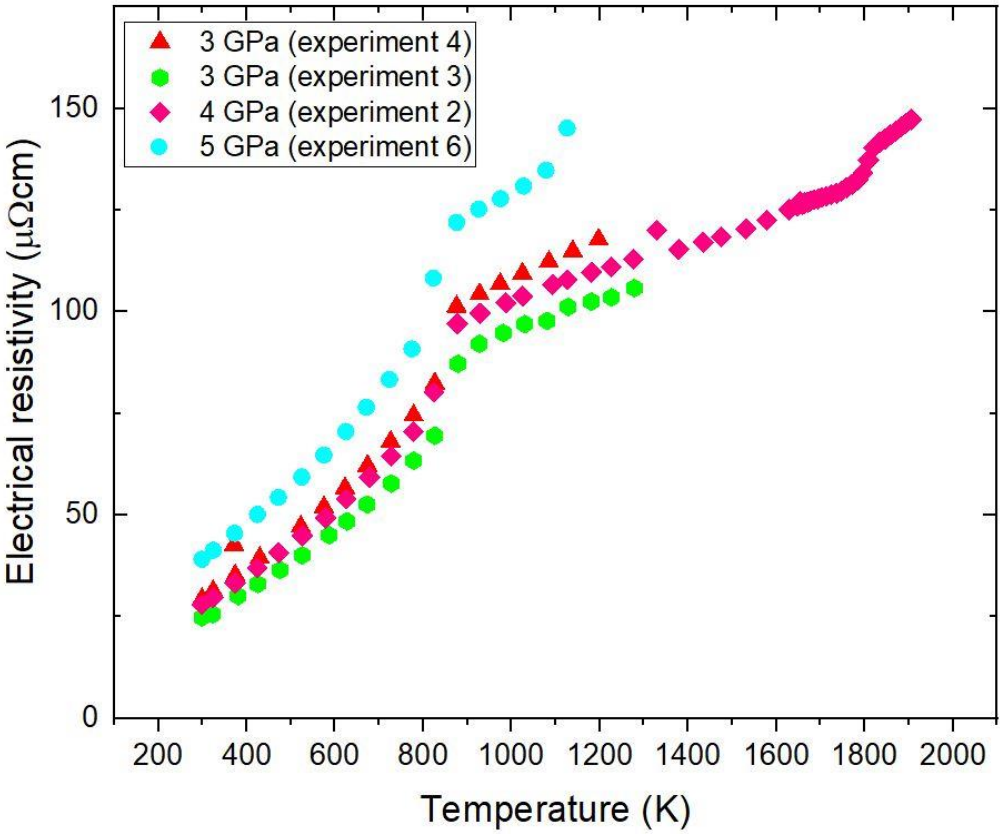

Figure 3.14: Electrical resistivity of the experiments conducted from 3-5 GPa at temperatures up to 1973 K.

Figure 3.15 is a plot comparing the electrical resistivity measurements gathered from Exp 2, 3, 4 and 6 in this study on Fe10Ni to pure Fe data at 3-5 GPa (Silber et al., 2018) and pure Ni data at 3-5 GPa (Silber et al., 2017), and Fe10Ni data at 4.5 GPa (Pommier, 2020) all using a multi-anvil press, and Fe10Ni data at high temperatures and ambient pressures by Ho et al (1983). The data collected in this study on Fe10Ni have a similar trend to the Fe data by Silber et al (2018), but with a slightly larger electrical resistivity throughout the temperature range.

The electrical resistivity of the measured data does not show a decrease with increasing pressure characteristic of most metals (Bridgman, 1952), but this could be due to contamination in the 5 GPa data, since it has considerably larger electrical resistivity values than the data at 3 and 4 GPa. There could also be geometry measurement related errors in the data due to incorrect measurements of the recovered samples and from pyrophyllite replacing the sample, making measurement of the recovered sample geometry inaccurate. There could also be errors in the 5 GPa data because BN was shown to have infiltrated into the sample tube at some point during the experiment. This could account for the slightly larger electrical resistivity values displayed throughout the data than the 4 and 3 GPa data. The measured data from this study also violates this rule when compared to the Fe10Ni data collected by Ho et al (1983). The data by Ho et al shows a similar trend but has lower electrical resistivity values than the electrical resistivity data that has been measured in this study. The data collected by Pommier (2020) at 4.5 GPa and temperatures above the melting point of Fe10Ni show electrical resistivity values larger than was found in this study. This could be because in her study, a powdered sample was used instead of a wire sample that was used in the present study. There is additional grain boundary scattering found in powders that is not found in wire samples used in studies such as this, leading to increases in electrical resistivity. The measurements in this study do show an increase in the electrical resistivity from the pure Fe and pure Ni data due to the impurity resistivity from the Fe and Ni alloying together. They also show that the impurity resistivity is additive and Matthiessen's law appears to hold for this alloy.

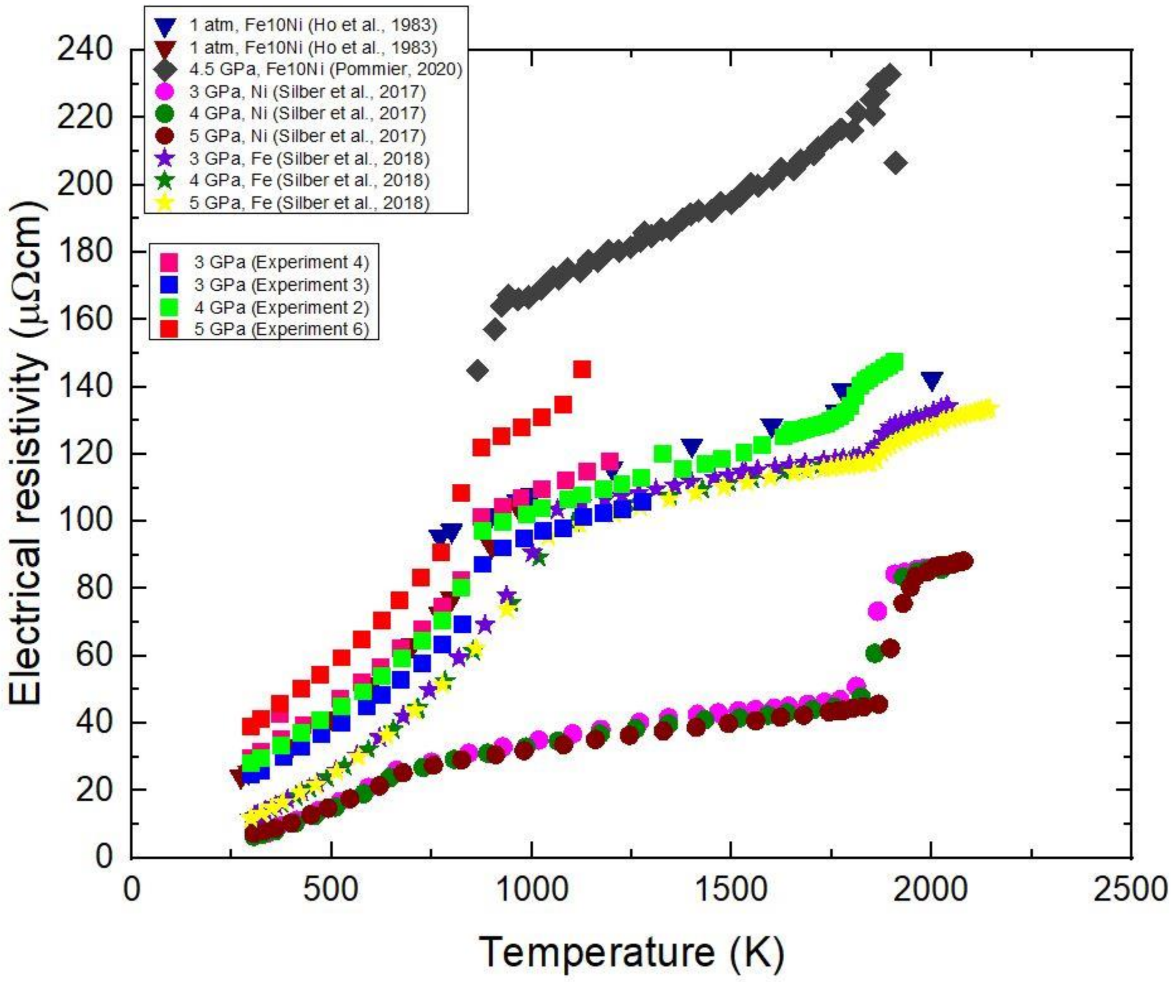

Figure 3.15: Electrical resistivity data for pure Fe and pure Ni at 3-5 GPa, Fe10Ni at 1 atm and Fe10Ni at 4.5 GPa in comparison to the experimentally measured data for Fe10Ni in this study.

3.8: Thermal conductivity

The thermal conductivity of the Fe10Ni alloy was calculated using the WFL (equation 2) with the Sommerfeld value used for the value of the Lorenz number. Figure 3.16 shows the thermal conductivity values of Exp 2, 3 ,4 and 6 plotted together. The thermal conductivity increases in the data with increasing temperature until 500 K, at which point the thermal conductivity decreases until reaching about the T_c of the alloy. From this point, magnon-electron scattering saturates, and electron-phonon scattering is more dominant, so the electrical resistivity plateaus. This means the thermal conductivity will increase more sharply from T_c, as it is inversely related to electrical resistivity. Data from Exp 2 shows the thermal conductivity increasing until reaching the melting temperature. After fully melting, the slope of the thermal conductivity data appears to be somewhat constant, so the electrical resistivity is increasing at the same rate as increasing temperature. The calculated thermal conductivity values are shown plotted in figure 3.17 with thermal conductivity data for Ni and Fe at 3, 4 and 5 GPa by Silber et al (2017) and Silber et al (2018). Thermal conductivity data at 4.5 GPa calculated using the WFL for Fe10Ni by Pommier (2020) is also included in this figure. The calculated thermal conductivity data from this study appears to follow the same trend as the Fe data, but with slightly lower thermal conductivity values. This is because of the impurity resistivity from Ni alloying causing the electrical resistivity to increase, inversely suppressing the thermal conductivity. The slope of the Ni conductivity data shows a sharp decrease with increasing temperature until T_c is reached. There is also a sharp decrease in conductivity at the melting point. These trends are not shown in the calculated thermal conductivity data and the Fe10Ni data follows the trends of the pure Fe data as expected. The Fe10Ni data from Pommier (2020) shows significantly lower thermal conductivity values than the data from this study. This could again be due to additional grain boundary scattering from the powdered sample.

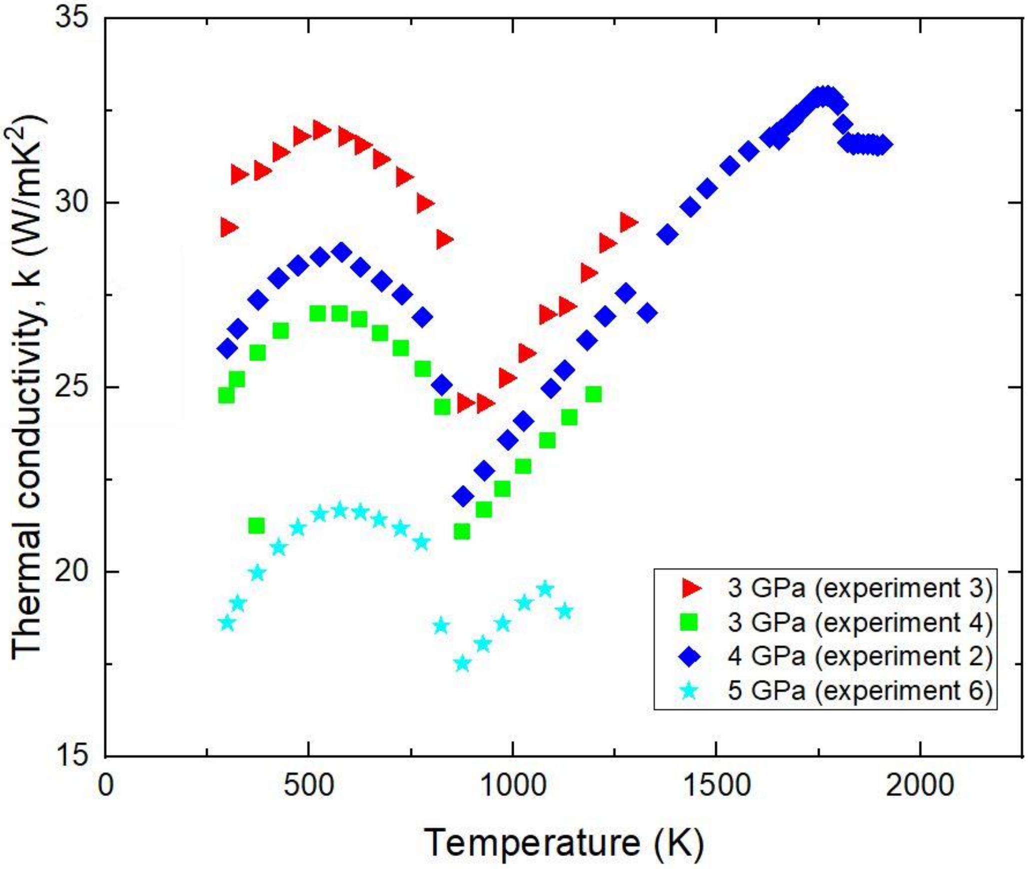

Figure 3.16: Thermal conductivity values calculated for Fe10Ni using the WFL and the measured electrical resistivity values.

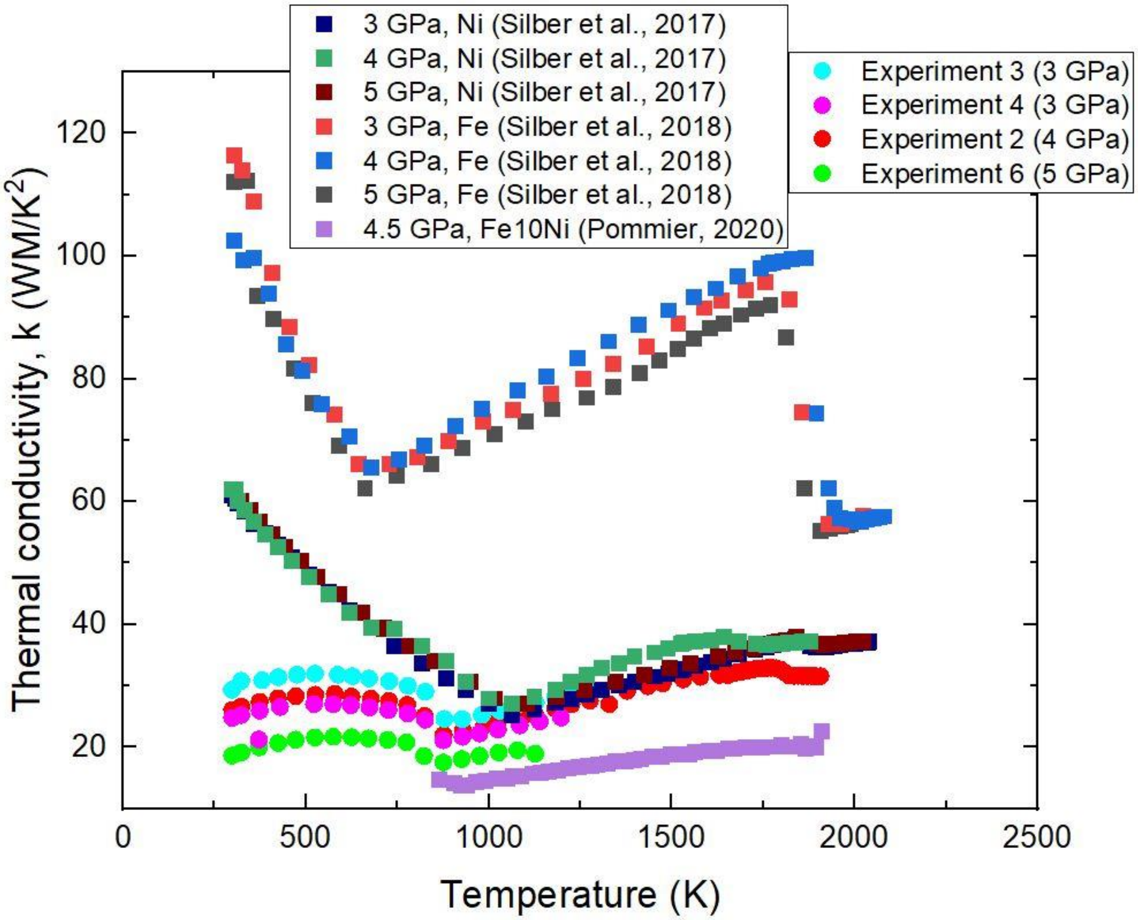

Figure 3.17: Thermal conductivity values for Fe10Ni for this study calculated using the WFL plotted with thermal conductivity values calculated by Pommier (2020), Silber et al. (2018) and Silber et al. (2017) for Fe10Ni, Fe and Ni, respectively.

3.9: Application to the lunar core

The adiabatic heat flux across the lunar CMB is given by:

$$q_{ad} = -k\frac{dT}{dr} \tag{8}$$

where $\frac{dT}{dr}$ is the temperature gradient and k is the thermal conductivity of the lunar OC. The temperature gradient is given by:

$$\left(\frac{dT}{dr}\right)_s = -\frac{2rT_{CMB}}{D^2} \tag{9}$$

where r is the radius of the lunar CMB, which is 330 km, T_{CMB} is the temperature at the lunar CMB, which is on average 1600 K. D is given by:

$$D = \sqrt{\frac{3C_{P,C}}{2\pi\alpha_C\rho_C G}} \tag{10}$$

where $C_{P,C}$ is the specific heat capacity at constant pressure, α_C is the thermal expansion, ρ_C is the density, and G is the gravitational constant. The values of the various parameters used in the calculation are shown in Table 3.1.

Table 3.1: Parameter values used to estimate the adiabatic heat flux across the lunar CMB. The larger values were used to calculate the upper limit for the adiabatic heat flow across the CMB and the smaller values were used to calculate the lower limit for the adiabatic heat flow across the CMB. The k value used was the thermal conductivity at 1600 K and 4 GPa.

Study	**r (km)**	**$C_{P,C}$ ($Jkg^{-1}K^{-1}$)**	**α_C ($10^{-5}K^{-1}$)**	**k ($Wm^{-1}K^{-1}$)**	**ρ_C (g/cm^3)**
This study	330	800-850	5.25-10	31.0	5-8
Berrada et al., (2020)	330	800-850	5.25-10	23.5-33.5	5-8
Silber et al., (2018)	N/A	800-850	5.25-10.3	33.5	N/A

Figure 3.18 is a plot of the q_{ad} at the top of the lunar core(1.5-3.0 mW/m^2) using the value of thermal conductivity calculated in this study and compared to a q_{ad} calculated using the thermal conductivity of pure Fe (Silber et al., 2018), Fe2Si, Fe8.5Si and Fe17Si (Berrada et al., 2020). The parameters used for all three studies are similar, with the only difference being the k value used for each of the studies. The 4 GPa thermal conductivity data was used in this calculation, since it does not have to be extrapolated to pressures significantly higher than 4

GPa to calculate the adiabatic heat flux at the top of the lunar core. The q_{ad} value calculated using the pure Fe k data by Silber et al is significantly larger than the value calculated in this study and by Berrada et al (2020) showing that small changes in the thermal conductivity can cause large variations in the calculated q_{ad} value and confirming that the effect of impurity resistivity due to alloying causes significant deviations from q_{ad} values calculated using pure Fe k data. The effect of alloying Fe with 10%wt Ni shows a similar effect to alloying Fe with 2%wt Si, despite a much larger amount being alloyed with Fe. This shows that Si alloying affects the thermal conductivity to a much greater extent than Ni alloying does, so constraining the thermal conductivity decrease caused by increasing Si wt% alloyed with Fe the correct amount is an important problem needing to be addressed. In order to do this, more research into the exact composition of the OC is needed to further guide experiments and simulations.

Laneuville et al (2018) calculated heat flux through the lunar CMB in five models. Their end member models for the heat flow through the CMB are presented in Fig. 3.18 as the two colored curves. When these models are combined with the results of the adiabatic heat flux at the top of the lunar core calculated in the current study, it indicates that the adiabatic heat flux at the top of the lunar core was less than the heat flux through the lunar CMB at times earlier than 3.7-3.45 Ga and thus thermal convection could have powered the lunar dynamo prior to 3.7-3.45 Ga. This is consistent with the conclusions of Berrada et al (2020) whose work on Fe-Si alloys showed similar adiabatic heat flux in the lunar core.

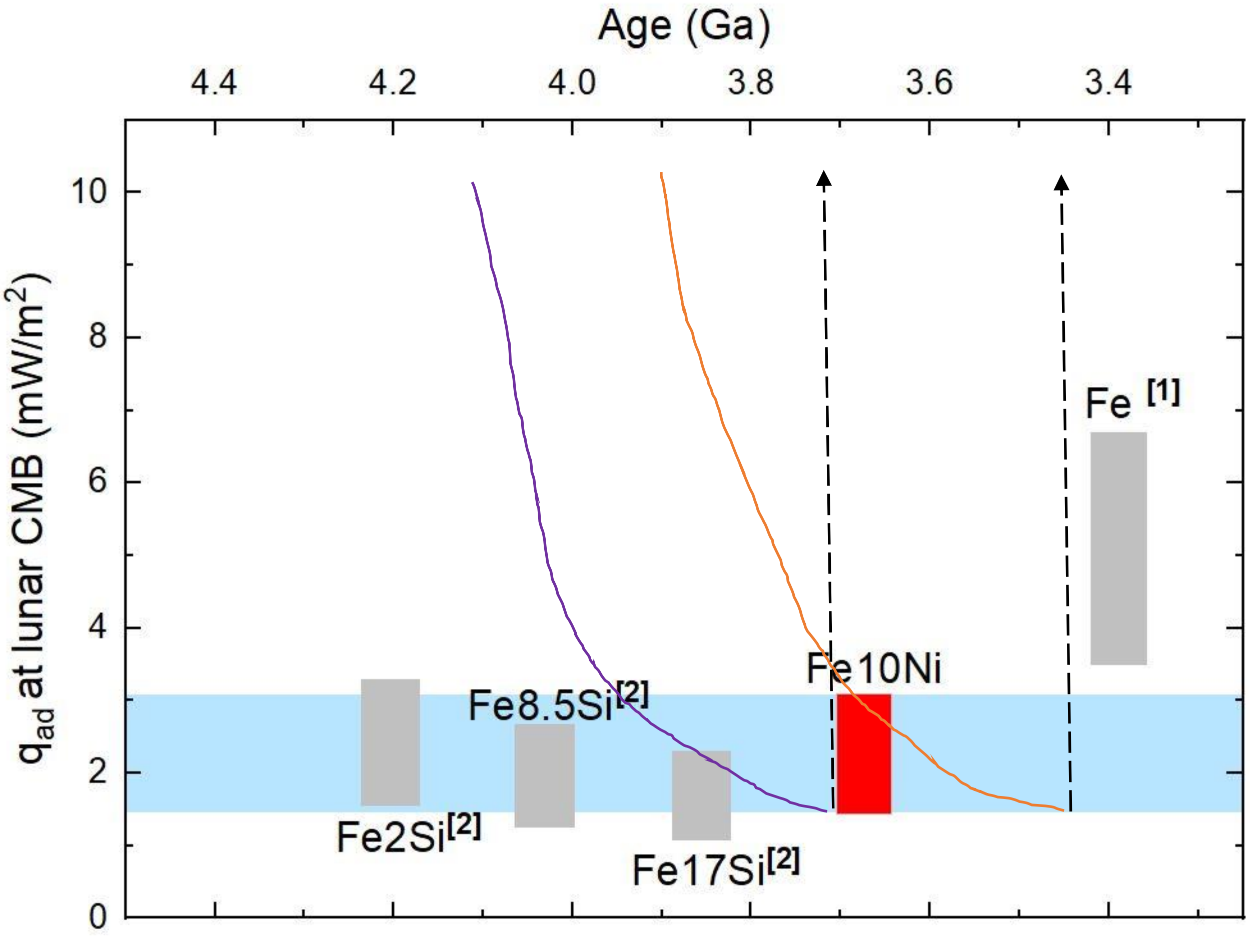

Figure 3.18: The q_{ad} at the lunar CMB calculated using the Fe10Ni data collected in this study is highlighted in red. This value was calculated to be 1.5-3.0 mW/m^2 for the upper and lower limits depending on parameter values used and is compared to values calculated using pure Fe thermal conductivity data and Fe-xSi. Reference [1] is Silber et al., 2018 and reference [2] is Berrada et al., 2020. The curved purple and orange lines are end-member model calculations of heat flow through the lunar CMB (Laneuville et al, 2018). The intersection of the end-member models and the lower range of heat flow calculated in the current study indicates that conducted heat flow was less than heat flow through the CMB (and therefore thermal convection may have operated) prior to at least 3.7 Ga and perhaps even prior to 3.45 Ga.

Chapter 4: Conclusions

The electrical resistivity of Fe10Ni was measured and thermal conductivity was calculated from data gathered at high pressure and high temperature using a 1000-ton cubic anvil press. Two cell designs were utilized after the first design had issues with sample containment at high temperatures. Design 2 did not fully solve the containment issues, and future research could be done to determine a design that will better contain the sample. The electrical resistivity shows similar trends to pure Fe data, with the impurity resistivity causing an increase in the electrical resistivity because of alloying with Ni. The data at 4 GPa shows an increase in electrical resistivity of around 10-15% due to melting of the alloy, in agreement with previous studies. More data above the melting temperature of the Fe-Ni alloy is necessary to determine if the electrical resistivity of the alloy is invariant along the melting curve as it is for Ni and Fe. If this is done, then extrapolations to the Earth's OC could be computed. The q_{ad} was calculated using the thermal conductivity data calculated in this study and was found to be 1.5-3.0 mW/m^2. This was compared with q_{ad} calculated using pure Fe and FexSi (2<x<17Si) thermal conductivity values and found to be lower than the value calculated using pure Fe and larger than the values calculated using FexSi. The adiabatic heat flux at the top of the lunar core calculated here is consistent with thermal convection as a power source of the lunar dynamo prior to 3.7-3.45 Ga.

Future work should include further research at higher pressures with varying compositions of Ni to determine the impact of increasing the concentration of Ni in the alloy will have on the electrical resistivity and the pressure dependence of the alloy, since this data showed that the electrical resistivity increased with increasing pressure, counter to what is expected. It would also be important to make measurements of resistivity in the liquid state at more than one pressure, as was done here, in order to determine if resistivity is constant along the melting boundary. A positive result would allow calculation of thermal conductivity, and adiabatic heat flow, at pressures higher than experiments. This could provide useful information on the possibility of thermal convection in liquid OC of larger terrestrial bodies such as Ganymede, Mercury and Mars.

References

Anderson, O. L. (1998). The Gruneisen parameter for iron at outer core conditions and the resulting conductive heat and power in the core. *Physics of the Earth and Planetary Interiors*, *109*(3–4), 179–197. DOI:10.1016/S0031-9201(98)00123-X

Berrada, M., Secco, R. A., Yong, W., Littleton, J. A. H. , (2020). Thermal convection in an early lunar dynamo from thermal conductivity study of Fe-Si. *Journal of Geophysical Research: Planets, submitted.*

Biggin, A. J., de Wit, M. J., Langereis, C. G., Zegers, T. E., Voûte, S., Dekkers, M. J., Drost, K. (2011). Palaeomagnetism of Archaean rocks of the Onverwacht Group, Barberton Greenstone Belt (southern Africa): Evidence for a stable and potentially reversing geomagnetic field at ca. 3.5Ga. *Earth and Planetary Science Letters*, *302*(3–4), 314–328. DOI:10.1016/j.epsl.2010.12.024

Bi, Y., Tan, H., Jing, F. (2002). Electrical conductivity of iron under shock compression up to 200 GPa. *Journal of Physics: Condensed Matter, 14*, 10849–10854.

Bridgman, P.W. (1952). The Resistance of 72 elements, alloys and compounds to 100 000 Kg/cm^2. *Proceedings of the American Academy of Arts and Sciences. 81*(4), 165-251

Buchwald, H. (1975). *Handbook of Iron Meteorites*, vol. 1 Chapter 8, Chemical Composition, pgs. 75–86.

Bullard, E. (1948). The secular change in the Earth’s magnetic field. *Geophysical Supplements to the Monthly Notices of the Royal Astronomical Society, 5*, 248–257.

Campbell, I. A., Fert, A. (1982). Transport properties of ferromagnets. *Ferromagnetic materials vol. 3.* North – Holland publishing company.

Chalmers, B. (1964). *Principles of solidification*. Wiley, New York.

Davies, C., Pozzo, M., Gubbins, D., Alfè, D. (2015). Constraints from material properties on the dynamics and evolution of Earth's core. *Nature Geoscience*, *8*(9), 678–685. DOI:10.1038/ngeo2492

de Koker, N., Steinle-Neumann, G., Vlcek, V. (2012). Electrical resistivity and thermal conductivity of liquid Fe alloys at high P and T, and heat flux in Earth's core. *Proceedings of the National Academy of the Sciences of the United States of America, 109,* 4070–4073.

Drchal, V., Kudrnovský, J., Wagenknecht, D., Turek, I., Khmelevskyi, S. (2017). Transport properties of iron at Earth's core conditions: The effect of spin disorder. *Physical Review B*, *96*(2), 1–16. DOI:10.1103/PhysRevB.96.024432

Dwyer, C. A., Stevenson, D. J., and Nimmo, F. (2011). A long-lived lunar dynamo driven by continuous mechanical stirring. *Nature, 479*(7372), 212-214. DOI:10.1038/nature10564

Elsasser, W. M. (1946). Induction effects in terrestrial magnetism part II. The secular variation. *Physical Review, 70,* 202.

Ezenwa, I. C., Secco, R. A. (2019). Fe melting transition: Electrical resistivity, thermal conductivity, and heat flow at the inner core boundaries of Mercury and Ganymede. *Crystals, 9*, 359. DOI:10.3390/cryst9070359

Fearn, D. R., Loper, D. E. (1981). Compositional convection and stratification of Earth's core. *Nature. 289,* 393-394

Garcia, R. F., Gagnepain-Beyneix, J., Chevrot, S., Lognonné, P. (2012). Erratum to "Very Preliminary Reference Moon Model", by Garcia, R. F., Gagnepain-Beyneix, J., Chevrot, S., Lognonné, P. [*Physics of the Earth and Planetary Interiors, 188* (2011) 96–113]. *Physics of the Earth and Planetary Interiors, 202-203,* 89-91. DOI: 10.1016/j.pepi.2012.03.009

Gardiner, R., Stacey, F. (1971). Electrical resistivity of the core. *Physics of the Earth and Planetary Interiors, 4,* 406–410.

Garrick-Bethell, I., Weiss, B. P., Shuster, D. L., Buz, J. (2009). Early lunar magnetism. *Science, 323*(5912), 356-359. DOI:10.1126/science.1166804

Gomi, H., Hirose, K. (2015). Electrical resistivity and thermal conductivity of hcp Fe– Ni alloys under high pressure: implications for thermal convection in the Earth's core. *Physics of the Earth and Planetary Interiors*, *247*, 2–10.

Gomi, H., Ohta, K., Hirose, K., Labrosse, S., Caracas, R., Verstraete, M. J., Herlund, J. W. (2013). The high conductivity of iron and thermal evolution of the Earth's core. *Physics of the Earth and Planetary Interiors*, *224*, 88–103.

Greim, J., Schwetz, K. (2005). Boron Carbide, Boron Nitride, and Metal Borides. In *Ullmann's Encyclopedia of Industrial Chemistry*. Edited by Barbara Elvers. John Wiley and Sons, Inc., New York, N.Y.

Gubbins, D., Alfè, D., Davies, C., Pozzo, M. (2015). On core convection and the geodynamo: Effects of high electrical and thermal conductivity. *Physics of the Earth and Planetary Interiors*, *247*, 56–64. DOI:10.1016/j.pepi.2015.04.002

Gunnarsson, O., Calandra, M., Han, J. E. (2003). Saturation of electrical resistivity. *Reviews of Modern Physics, 75,* 1085–1099.

Hicks, T. L., Secco, R. A. (1997). Dehydration and decomposition of pyrophyllite at high pressures: electrical conductivity and X-ray diffraction studies to 5 GPa. *Canadian Journal of Earth Sciences, 34,* 875-882.

Ho, C. Y., Ackerman, M. W., Wu, K. Y., Havill, T. N., Bogaard, R. H., Matula, S. G., James, H. M. (1983). Electrical resistivity of ten selected binary alloy systems*. Journal of Physical Chemistry Reference Data, 12*(2).

Ioffe, A. F., Regel. A. R. (1960). Non-crystalline, amorphous and liquid electronic semiconductors. *Progress in Semiconductors, 4*, 237-291.

Ito, E. (2007). Theory and Practise – Multianvil Cells and High-Pressure Experimental Methods. *Treatise on Geophysics.* Edited by G. David Price and Gerald Schubert. Elsevier Ltd., Waltham, Wt. 197-230.

Jain, A., Evans, R. (1972). Calculation of the electrical resistivity of liquid iron in the earth's core. *Nature, 235*, 165–167.

Kittel, C. (2005). Introduction to Solid State Physics. John Wiley and Sons Inc., Hoboken. 681 pgs.

Konôpková, Z., McWilliams, R. S., Gómez-Pérez, N., Goncharov, A. F. (2016). Direct measurement of thermal conductivity in solid iron at planetary core conditions. *Nature*, *534*, 99–101. DOI:10.1038/nature18009

Kubaschewski, O. (1982). *Iron – binary phase diagrams*. Springer – Verlag, Berlin.

Labrosse, S. (2015). Thermal evolution of the core with a high thermal conductivity. *Physics of the Earth and Planetary Interiors*, *247*, 36–55. DOI:10.1016/j.pepi.2015.02.002

Laneuville, M., Taylor, J., Wieczorek, M. A. (2018). Distribution of Radioactive Heat Sources and Thermal History of the Moon. *Journal of Geophysical Research: Planets, 123*(12), 3144-3166. DOI: 10.1029/2018JE005742

Lay, T., Hernlund, J., Buffett, B.A. (2008). Core–mantle boundary heat flow. *Nature Geoscience, 1,* 25–32

Matassov, G. (1977). The electrical conductivity of iron-silicon alloys at high pressures and the Earth's core. PhD Thesis, Lawrence Livermore National Laboratory, Univ. California.

McDonough, W. F., Sun, S. (1995). The composition of the Earth. *Chemical geology, 120*, 223-253.

Nimmo, F., Price, G. D., Brodholt, J., Gubbins, D. (2004). The influence of potassium on core and geodynamo evolution. *Geophysical Journal International*, *156*(2), 363–376. DOI:10.1111/j.1365-246X.2003.02157.x

Nielsen, R., Chang, T. (2005). Zirconium and Zirconium Compounds. In *Ullmann's Encyclopedia of Industrial Chemistry*. Edited by Barbara Elvers. John Wiley and Sons, Inc., New York, N.Y.

Pollock, D. (1991). *Thermocouples: Theory and properties*. CRC press. pgs. 249.

Pommier, A. (2020). Experimental Investigation of the Effect of Nickel on the Electrical Resistivity of Fe-Ni and Fe-Ni-S Alloys under Pressure. *American Mineralogist, In press.*

Pozzo, M., Davies, C., Gubbins, D., Alfè, D. (2012). Thermal and electrical conductivity of iron at Earth's core conditions. *Nature*, *485*, 355–358. DOI:10.1038/nature11031

Reed, S. (2005). *Electron Microprobe Analysis and Scanning Electron Microscopy in Geology*, *Second Edition.* Cambridge University Press, New York, N.Y.

Scheinberg, A., Soderlund, K. M., and Schubert, G. (2015). Magnetic field generation in the lunar core: The role of inner core growth. *Icarus, 254*, 62-71. DOI:10.1016/j.icarus.2015.03.013

Seagle, C. T., Cottrell, E., Fei, Y., Hummer, D. R., Prakapenka. V. B. (2013). *Geophysical Research Letters*, *40*, 5377–5381. DOI:10.1002/2013GL057930

Secco, R., Schloessin, H. (1989). The electrical resistivity of solid and liquid Fe at pressures up to 7 GPa. *Journal of Geophysical Research, 94,* 5887–5894.

Secco, R. A. (2017). Thermal conductivity and Seebeck coefficient of Fe and Fe-Si alloys: Implications for variable Lorenz number. *Physics of the Earth and Planetary Interiors*, *265*, 23–34. DOI:10.1016/j.pepi.2017.01.005

Shea, E. K., Weiss, B. P., Cassata, W. S., et al. (2012). A long-lived lunar core dynamo. *Science. 335*(6067), 453-456. DOI:10.1126/science.1215359

Silber, R. E., Secco, R. A., Yong, W. (2017). Constant electrical resistivity of Ni along the melting boundary up to 9 GPa. *Journal of Geophysical Research: Solid Earth*, *122*(7), 5064–5081. DOI:10.1002/2017JB014259

Silber, R. E., Secco, R. A., Yong, W., Littleton, J. A. H. (2018). Electrical resistivity of liquid Fe to 12 GPa: Implications for heat flow in cores of terrestrial bodies. *Scientific Reports*, *8*(1), 1–9. DOI:10.1038/s41598-018-28921-w

Stacey, F., Anderson, O. (2001). Electrical and thermal conductivities of Fe-Ni-Si alloy under core conditions. *Physics of the Earth and Planetary Interiors*, *124*, 153–162.

Stacey, E.D., Loper, D. (1983). The thermal boundary layer interpretation of D’’ and its role as a plume source. *Physics of the earth and planetary interiors. 33,* 45-55

Stacey, F., Loper, D. (2007). A revised estimate of the conductivity of iron alloy at high pressure and implications for the core energy balance. *Physics of the Earth and Planetary Interiors*, *161*, 13–18.

Stevenson, D. J. (2003). Planetary magnetic fields. *Earth and Planetary Science Letters*, *208*, 1–11. DOI:10.1088/0034-4885/46/5/001

Suavet, C., Weiss, B. P., Cassata, W. S., et al. (2013). Persistence and origin of the lunar core dynamo. *Proceedings of the National Academy of Sciences, 110*(21), 8453-8458. DOI:10.1073/pnas.1300341110

Tarduno, J. A., Cottrell, R. D., Davis, W. J., Nimmo, F. & Bono, R. K. (2015). A Hadean to Paleoarchean geodynamo recorded by single zircon crystals. *Science, 349*, 521–524.

Tateno, S., Hirose, K., Ohishi, Y., Tatsumi, Y. (2010). The structure of iron in Earth's inner core. *Science, 330,* 359–361.

Uher, C. (2004). Thermal conductivity of metals. In T.M. Tritt (Ed.). *Thermal conductivity: Theory, properties, and applications.* New York: Plenum publishers.

Watanabe, M., Adachi, M., Uchikoshi, M., Fukuyama, H. (2019). Thermal Conductivities of Fe-Ni Melts Measured by Non-contact Laser Modulation Calorimetry. *Metallurgical and Materials Transactions, (50A)*. 3295-3300

Weber, R. C., Lin, P. Y., Garnero, E. J., Williams, Q., and Lognonné, P. (2011). Seismic Detection of the Lunar Core. *Science, 331*(6015), 309-312. DOI:10.1126/science.1199375

Wieczorek, M., Jolliff, B., Khan, A., et al. (2006). *The Constitution and Structure of the Lunar Interior*. *Reviews in mineralogy and geochemistry*, *60*(1), 221-364.

Wiedemann, D., Franz, R. (1853). Ueber die Wärme-Leitungsfähigkeit der Metalle. *Ann. Phys. Chem. 89,* 497–531.

Williamson, E. D., Adams, L. H. (1923). Density distribution in the Earth. *Journal of Washington Academy of Sciences: 13:* 413-432

Williams, Q. (2018). The Thermal Conductivity of Earth's Core: A Key Geophysical Parameter's Constraints and Uncertainties. *Annual Review of Earth and Planetary Sciences*, *46*(1), 47–66. DOI:10.1146/annurev-earth-082517-010154

Xu, J., Zhang, P., Haule, K., Minar, J., Wimmer, S., Ebert, H., & Cohen, R. E. (2018). Thermal Conductivity and Electrical Resistivity of Solid Iron at Earth's Core Conditions from First Principles. *Physical Review Letters*, *121*(9), 96601. DOI: 10.1103/PhysRevLett.121.096601

Yong, W., Secco, R. A., Littleton, J. A. H., & Silber, R. E. (2019). The iron invariance: Implications for thermal convection in Earth's core. *Geophysical Research Letters, 46*.

DOI: 10.1029/2019GL084485

Zhang, Y., Nelson, P., Dygert, N., Lin, J. (2019). Fe alloy slurry and a compacting cumulate pile across Earth's inner-core boundary. *Journal of Geophysical Research*

Appendix

EMPA of sample 1 – Wt%

Nd = not detected

Points are shown in an image for each EMPA in the results and conclusion section with labels

Point	Additional comments (e.g. part probed)	Si(Wt%)	Fe(Wt%)	Ni(Wt%)	Re(Wt%)	W(Wt%)	Total(Wt%)
1	1_01	0.058	nd	0.026	25.41	72.727	98.221
2	1_02	0.057	nd	0.029	0.251	98.252	98.589
3	1_03	nd	66.202	8.751	1.742	20.379	97.074
4	1_04	0.024	21.447	2.287	6.135	66.411	96.304
5	1_05	0.059	0.01	0.021	0.253	98.262	98.605
6	1_06	nd	64.081	8.787	0.282	24.148	97.298
7	1_07	0.056	29.829	2.262	1.5	65.274	98.921
8	1_08	0.064	0.036	0.042	0.193	99.407	99.742
9	1_09	nd	63.002	8.497	0.408	25.128	97.035
10	1_10	0.043	29.487	2.259	1.22	65.59	98.599
11	1_11	nd	63.95	8.983	0.198	23.913	97.044
12	1_12	0.061	32.688	2.836	0.834	62.03	98.449
13	1_13	nd	63.692	8.954	0.198	24.362	97.206
14	1_14	0.028	30.409	2.251	1.298	65.076	99.062
15	1_15	nd	65.119	8.886	0.233	23.475	97.713
16	1_16	0.027	30.963	2.417	1.575	64.075	99.057
17	1_17	nd	54.252	6.863	0.281	36.636	98.032
18	1_18	0.015	52.579	6.691	0.381	39.068	98.734
19	1_19	nd	65.072	8.698	0.26	23.183	97.213
20	1_20	0.047	30.811	2.189	1.377	64.343	98.767
21	1_21	nd	65.149	8.478	0.49	23.12	97.237
22	1_22	0.022	30.327	2.154	2.103	64.302	98.908
23	1_23	nd	64.807	9.218	0.153	23.17	97.348
24	1_24	0.037	30.632	2.293	1.477	64.513	98.952
25	1_25	nd	65.818	8.581	0.25	22.739	97.388
26	1_26	nd	59.22	7.502	0.402	31.579	98.703
27	1_27	nd	64.559	8.443	0.631	23.628	97.261
28	1_28	0.05	30.127	2.149	2.674	64.133	99.133
29	1_29	nd	65.27	8.394	0.593	23.164	97.421
30	1_30	0.034	31.088	2.219	2.627	62.719	98.687
31	1_31	nd	65.131	8.31	0.461	23.163	97.065
32	1_32	0.034	34.363	2.706	1.908	59.961	98.972
33	1_33	nd	63.525	8.573	0.373	24.362	96.833

34	1_34	0.058	29.324	2.094	2.916	64.433	98.825
35	1_35	0.02	56.294	7.214	0.42	34.054	98.002
36	1_36	0.053	30.161	2.209	2.99	63.339	98.752
37	1_37	nd	65.755	8.36	0.477	22.529	97.121
38	1_38	0.024	29.713	2.027	2.394	64.317	98.475
39	1_39	nd	64.502	8.64	0.525	23.456	97.123
40	1_40	0.039	30.411	2.215	2.607	63.607	98.879
41	1_41	nd	63.779	8.407	0.467	24.247	96.900
42	1_42	0.054	32.395	2.609	2.425	61.086	98.569
43	1_43	nd	64.142	8.366	0.575	24.329	97.412
44	1_44	0.055	29.865	2.072	2.506	63.87	98.368
45	1_45	0.066	0.021	0.033	0.197	97.808	98.125
46	1_46	nd	62.353	8.354	0.569	26.049	97.325
47	1_47	0.076	28.645	1.998	3.448	65	99.167
48	1_48	0.047	0.018	0.056	0.227	97.912	98.260
49	1_49	0.055	nd	0.014	25.392	73.296	98.757

EMPA of sample 1 – Atomic %

Point	Additional comments (e.g. part probed)	Si(Atom %)	Fe(Atom%)	Ni(Atom%)	Re(Atom%)	W(Atom%)	Total(Atom%)
1	1_01	0.383	-0.0411	0.0814	25.5306	74.005	99.2044
2	1_02	0.3782	-0.0493	0.0932	0.2502	99.2784	99.7409
3	1_03	-0.0677	81.4896	10.2471	0.6431	7.6202	99.8513
4	1_04	0.1062	46.9441	4.7628	4.0281	44.1588	99.8083
5	1_05	0.387	0.0326	0.0653	0.2523	99.2628	99.7696
6	1_06	-0.0395	80.2411	10.4674	0.106	9.1856	99.8809
7	1_07	0.2137	56.9561	4.1092	0.8592	37.8618	99.8543
8	1_08	0.4197	0.1189	0.1316	0.1901	99.1397	99.7731
9	1_09	-0.0986	79.9108	10.2521	0.1551	9.682	99.8633
10	1_10	0.1633	56.6924	4.1323	0.7038	38.3081	99.8896
11	1_11	-0.0698	80.1184	10.7063	0.0743	9.101	99.8231
12	1_12	0.2211	59.8682	4.941	0.4583	34.5114	99.8768
13	1_13	-0.0978	79.9451	10.6909	0.0745	9.2894	99.8604
14	1_14	0.1056	57.6319	4.0588	0.7376	37.466	99.9026
15	1_15	-0.1021	80.6195	10.4654	0.0865	8.8286	99.8659
16	1_16	0.1005	58.143	4.3174	0.8871	36.552	99.9384
17	1_17	-0.0239	75.3559	9.0685	0.117	15.4586	99.8954
18	1_18	0.0417	74.1007	8.9709	0.1609	16.7258	99.8895
19	1_19	-0.0564	80.8684	10.2823	0.097	8.7522	99.9131
20	1_20	0.1776	58.1929	3.9328	0.7802	36.9165	99.8875
21	1_21	-0.1194	81.0466	10.0332	0.1827	8.7375	99.8436
22	1_22	0.0842	57.6724	3.8968	1.1995	37.1471	99.8817
23	1_23	-0.0575	80.3451	10.8716	0.0571	8.7262	99.898
24	1_24	0.1378	57.8765	4.121	0.8368	37.0279	99.8494
25	1_25	-0.067	81.2927	10.0827	0.0926	8.5319	99.9177
26	1_26	-0.0275	77.849	9.3817	0.1585	12.6107	99.9611
27	1_27	-0.0835	80.7411	10.0453	0.2369	8.9767	99.8286
28	1_28	0.1873	57.3257	3.8905	1.5261	37.0704	99.9068
29	1_29	-0.0546	81.1111	9.9235	0.2209	8.7444	99.8713
30	1_30	0.127	58.5385	3.9742	1.4839	35.8764	99.8609
31	1_31	-0.0939	81.1999	9.8553	0.1723	8.7726	99.8567
32	1_32	0.1222	61.5906	4.6139	1.0259	32.6475	99.8604
33	1_33	-0.0512	80.2157	10.2978	0.1412	9.3453	99.9263
34	1_34	0.2206	56.5244	3.8393	1.686	37.7298	99.8597
35	1_35	0.0546	76.4164	9.3151	0.1711	14.0428	99.9029

36	1_36	0.201	57.443	4.0029	1.708	36.6451	99.8619
37	1_37	-0.0719	81.4856	9.8556	0.1774	8.4813	99.8524
38	1_38	0.0908	57.201	3.7127	1.3826	37.6129	99.8948
39	1_39	-0.0536	80.6238	10.273	0.1967	8.9065	99.8724
40	1_40	0.1473	57.705	3.9985	1.484	36.6653	99.8279
41	1_41	-0.0757	80.4458	10.087	0.1766	9.2906	99.8565
42	1_42	0.1967	59.695	4.5733	1.3403	34.1947	99.8617
43	1_43	-0.0851	80.5166	9.9896	0.2165	9.2772	99.8623
44	1_44	0.2099	57.3225	3.7839	1.4428	37.2409	99.8607
45	1_45	0.4378	0.0701	0.105	0.197	99.1902	99.8005
46	1_46	-0.0532	79.548	10.1387	0.2178	10.0954	99.8662
47	1_47	0.2922	55.6478	3.6916	2.0089	38.3595	99.8887
48	1_48	0.314	0.0617	0.1778	0.2274	99.219	99.9185
49	1_49	0.362	-0.0097	0.044	25.3844	74.2095	99.3596

EMPA of sample 5 – Wt %

Point	Additional comments (e.g. part probed)	Fe(Wt%)	Ni(Wt%)	Re(Wt%)	W(Wt%)	Total(Wt%)
1	5_01	90.889	9.552	nd	nd	100.441
2	5_02	90.522	9.808	nd	nd	100.330
3	5_03	91.175	9.73	nd	nd	100.905
4	5_04	90.35	9.539	nd	0.014	99.903
5	5_05	89.924	9.81	nd	nd	99.734
6	5_06	89.903	9.516	nd	nd	99.419
7	5_07	90.218	9.553	nd	nd	99.771
8	5_08	89.8	9.647	nd	nd	99.447
9	5_09	89.767	9.705	nd	nd	99.472
10	5_thermocouple_above	nd	0.01	5.285	94.106	99.401
11	5_thermocouple_below1	nd	0.004	26.031	73.956	99.991
12	5_thermocouple_below2	nd	0.049	5.003	94.465	99.517

EMPA of sample 5 – Atomic %

Point	Additional comments (e.g. part probed)	Fe(Atom%)	Ni(Atom%)	Re(Atom%)	W(Atom%)	Total(Atom%)
1	5_01	90.9114	9.0886	-0.0134	-0.0123	99.9743
2	5_02	90.6558	9.3442	-0.0235	-0.0059	99.9706
3	5_03	90.7835	9.2165	-0.015	-0.0003	99.9847
4	5_04	90.8692	9.1267	-0.018	0.0042	99.9821
5	5_05	90.5979	9.4021	-0.0178	-0.0026	99.9796
6	5_06	90.8522	9.1478	-0.0155	-0.0082	99.9763
7	5_07	90.8484	9.1516	-0.0221	-0.0057	99.9722
8	5_08	90.7282	9.2718	-0.021	-0.0045	99.9745
9	5_09	90.6742	9.3258	-0.0117	-0.0036	99.9847
10	5_thermocouple_above	-0.0165	0.0308	5.2525	94.7167	99.9835
11	5_thermocouple_below1	-0.0324	0.0141	25.7868	74.1992	99.9677
12	5_thermocouple_below2	-0.0311	0.1541	4.9617	94.8843	99.969

EMPA of sample 6 – Wt %

Point	Additional comments (e.g. part probed)	Fe(Wt%)	Ni(Wt%)	Re(Wt%)	W(Wt%)	Total(Wt%)
13	6_01	nd	0.026	0.161	99.643	99.830
14	6_02	61.235	6.551	nd	31.986	99.772
15	6_03	60.464	6.414	0.001	32.049	98.928
16	6_04	58.38	6.162	0.05	34.847	99.439
17	6_05	72.767	7.775	nd	18.911	99.453
18	6_06	69.438	7.425	0.009	22.069	98.941
19	6_07	75.989	8.129	nd	15.809	99.927
20	6_08	74.068	7.808	0.024	17.771	99.671
21	6_09	76.77	8.091	0.013	14.986	99.860
22	6_10	76.89	8.258	nd	13.792	98.940
23	6_11	78.219	8.457	nd	12.229	98.905
24	6_12	75.478	7.981	0.052	16.047	99.558
25	6_13	77.066	8.234	nd	13.573	98.873
26	6_14	72.08	7.735	0.695	19.482	99.992
27	6_15	63.038	6.48	1.083	28.93	99.531
28	6_16	76.078	8.151	0.042	14.625	98.896
29	6_17	66.56	7.138	1.421	24.666	99.785
30	6_18	71.208	7.687	0.791	20.257	99.943
31	6_19	73.308	7.88	0.095	17.804	99.087
32	6_20	59.737	6.071	1.864	31.879	99.551
33	6_21	67.736	7.228	0.887	23.936	99.787
34	6_22	74.867	8.162	0.048	15.678	98.755
35	6_23	63.982	6.75	1.8	26.598	99.130
36	6_24	70.879	7.77	0.433	19.713	98.795
37	6_25	74.443	8.058	0.073	16.689	99.263
38	6_26	65.834	7.011	1.663	25.463	99.971
39	6_27	71.069	7.849	0.674	19.183	98.775
40	6_28	75.549	8.231	0.062	15.308	99.150
41	6_29	66.935	7.255	1.759	23.824	99.773
42	6_30	65.918	7.144	0.819	25.434	99.315
43	6_31	64.023	6.985	0.865	27.33	99.203
44	6_32	nd	0.051	0.1	99.267	99.418
45	6_33	0.015	0.02	0.154	99.661	99.850
46	6_34	0.005	0.029	25.811	74.27	100.115

EMPA of sample 6 – Atomic %

Point	Additional comments (e.g. part probed)	Fe(Atom%)	Ni(Atom%)	Re(Atom%)	W(Atom%)	Total(Atom%
13	6_01	-0.0304	0.0803	0.1592	99.7605	99.9696
14	6_02	79.337	8.0737	-0.0103	12.5893	99.9897
15	6_03	79.2428	7.997	0.0004	12.7598	100
16	6_04	78.004	7.8319	0.02	14.1441	100
17	6_05	84.703	8.61	-0.0124	6.6871	99.9877
18	6_06	83.4509	8.4889	0.0031	8.0571	100
19	6_07	85.8392	8.7358	-0.0065	5.425	99.9935
20	6_08	85.2324	8.5469	0.0084	6.2123	100
21	6_09	86.2354	8.6463	0.0044	5.1138	99.9999
22	6_10	86.4558	8.8331	-0.0055	4.7111	99.9945
23	6_11	86.9303	8.941	-0.0101	4.1286	99.9898
24	6_12	85.8085	8.6318	0.0178	5.5418	99.9999
25	6_13	86.5694	8.7988	-0.0079	4.6318	99.9921
26	6_14	84.2405	8.5992	0.2436	6.9167	100
27	6_15	80.4923	7.8713	0.4147	11.2217	100
28	6_16	86.1707	8.783	0.0142	5.0321	100
29	6_17	81.9008	8.355	0.5243	9.2199	100
30	6_18	83.8618	8.6116	0.2793	7.2473	100
31	6_19	85.0039	8.6918	0.0329	6.2714	100
32	6_20	78.8549	7.6235	0.7382	12.7834	100
33	6_21	82.4547	8.37	0.324	8.8513	100
34	6_22	85.6518	8.8828	0.0166	5.4488	100
35	6_23	80.9663	8.1258	0.6833	10.2246	100
36	6_24	83.9912	8.7587	0.1539	7.0962	100
37	6_25	85.3703	8.7907	0.0251	5.8139	100
38	6_26	81.5403	8.2611	0.6179	9.5807	100
39	6_27	84.0406	8.8292	0.2392	6.8909	99.9999
40	6_28	85.805	8.8925	0.021	5.2814	99.9999
41	6_29	82.0269	8.4573	0.6466	8.8692	100
42	6_30	81.6968	8.4229	0.3046	9.5757	100
43	6_31	80.8072	8.3868	0.3273	10.4787	100
44	6_32	-0.0444	0.1607	0.0995	99.7398	99.9556
45	6_33	0.0508	0.0638	0.1521	99.7333	100
46	6_34	0.0156	0.0915	25.5205	74.3724	100

Exp 1 (recovered from 4 GPa, 1973 K) – EDS

1_01

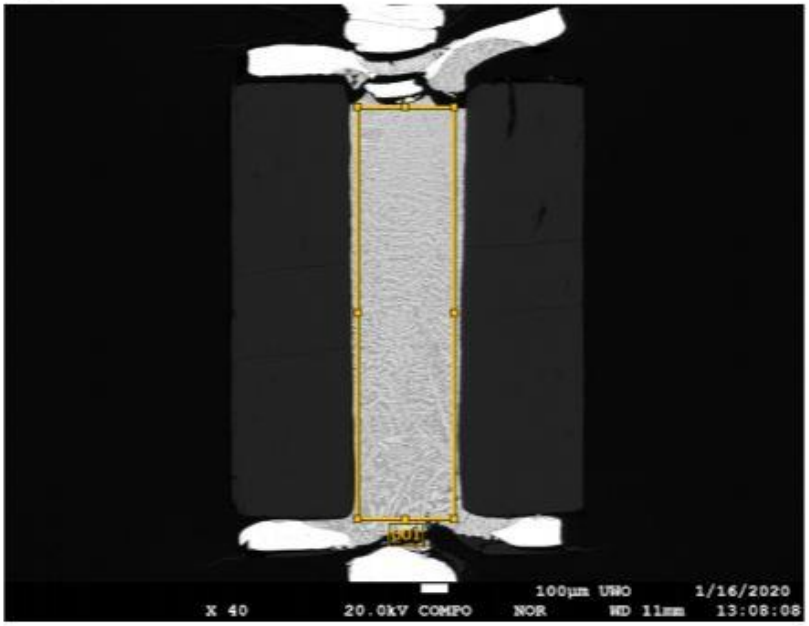

```
Volt            : 20.00 kV
Mag.            : x 40
Date            : 2020/01/16
Pixel           : 1280 x 960
```

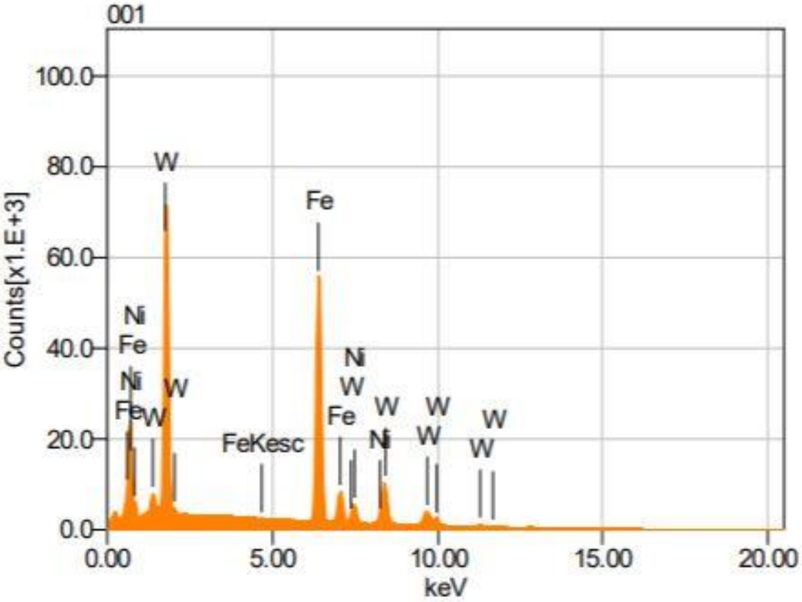

```
Acquisition Condition
Instrument      : 8530F
Volt            : 20.00 kV
Current         : ---
Process Time    : T2
Live time       : 60.00 sec.
Real Time       : 98.79 sec.
DeadTime        : 39.00 %
Count Rate      : 83246.00 CP
```

```
Formula         mass%   Atom%   Sigma   Net             K ratio         Line
Fe              49.24   71.80   0.03    29577349        25.6440212      K
Ni              6.06    8.40    0.02    2547130         3.0761565       K
W               44.70   19.80   0.07    25613352        14.7931634      M
Total           100.00  100.00
```

1_02

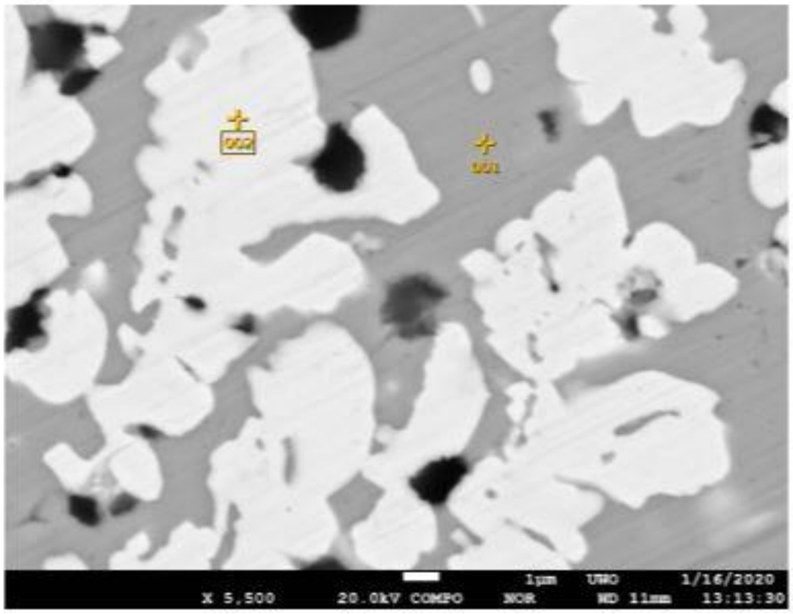

Volt : 20.00 kV
Mag. : x 5,500
Date : 2020/01/16
Pixel : 1280 x 960

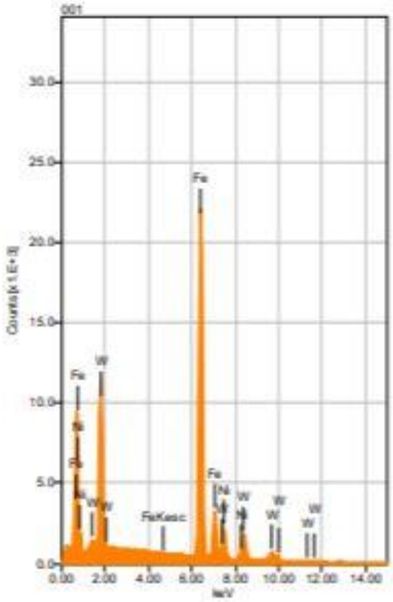

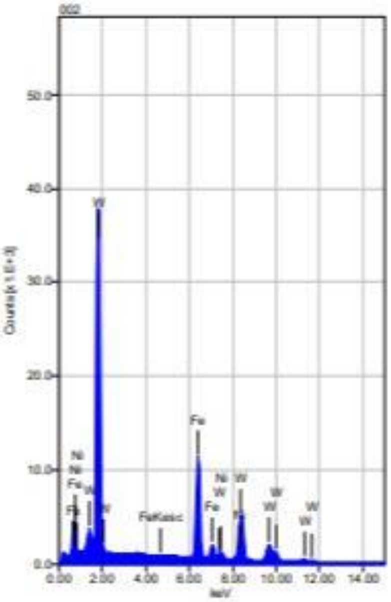

Acquisition Condition
Instrument : 8530F
Volt : 20.00 kV
Current : ---
Process Time : T2
Live time : 18.90 sec.
Real Time : 33.38 sec.
DeadTime : 44.00 %
Count Rate : 94760.00 CP

	Fe	Ni	W
001	65.60	9.57	24.83
002	30.07	2.66	67.27
Average	47.84	6.11	46.05
Deviation	25.12	4.88	30.01

<u>Exp 2 (recovered from 4 GPa, 1920 K) - EDS</u>

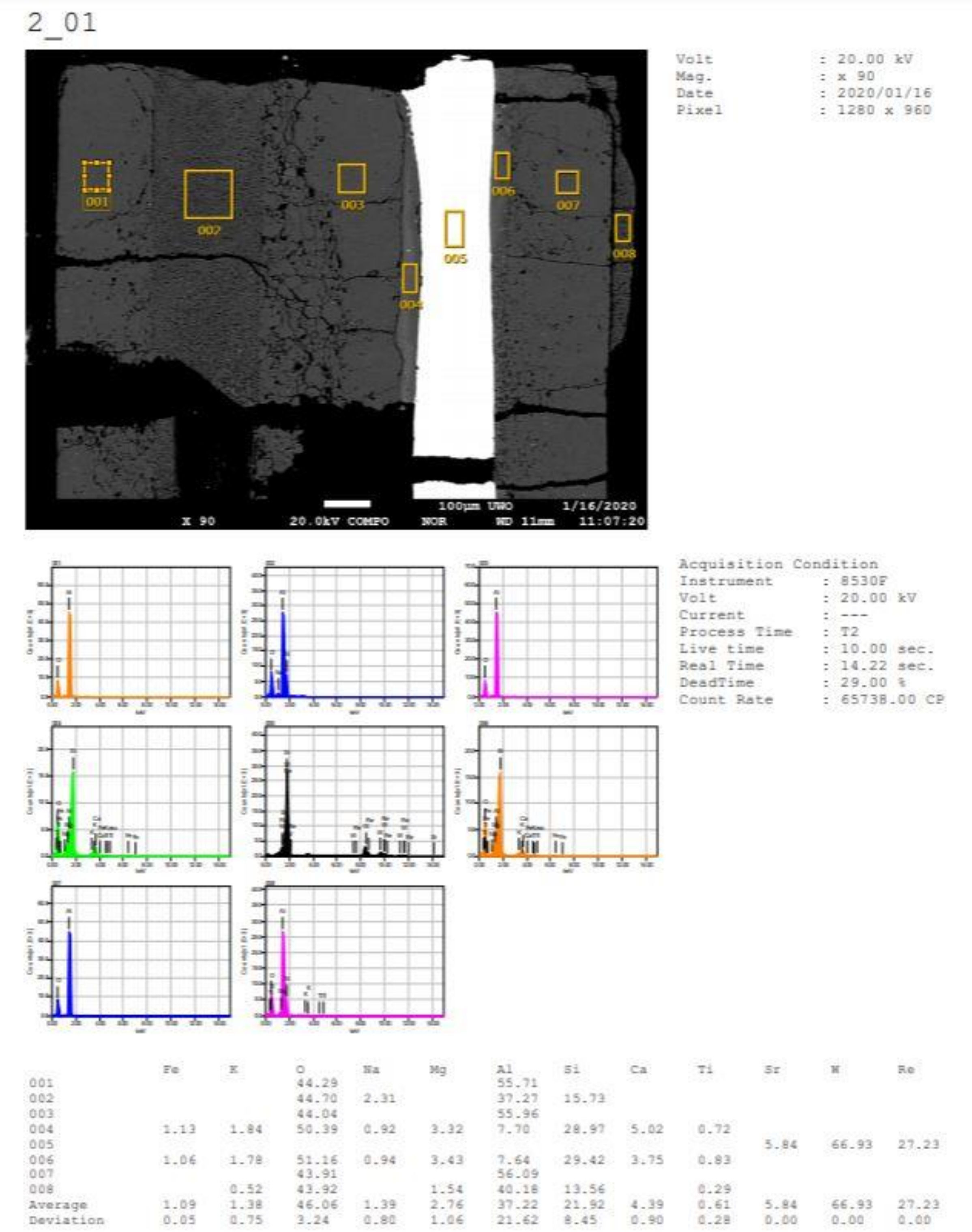

2_01

Volt	: 20.00 kV
Mag.	: x 90
Date	: 2020/01/16
Pixel	: 1280 x 960

Acquisition Condition

Instrument	: 8530F
Volt	: 20.00 kV
Current	: ---
Process Time	: T2
Live time	: 10.00 sec.
Real Time	: 14.22 sec.
DeadTime	: 29.00 %
Count Rate	: 65738.00 CP

	Fe	K	O	Na	Mg	Al	Si	Ca	Ti	Sr	W	Re
001			44.29			55.71						
002			44.70	2.31		37.27	15.73					
003			44.04			55.96						
004	1.13	1.84	50.39	0.92	3.32	7.70	28.97	5.02	0.72			
005										5.84	66.93	27.23
006	1.06	1.78	51.16	0.94	3.43	7.64	29.42	3.75	0.83			
007			43.91			56.09						
008		0.52	43.92		1.54	40.18	13.56		0.29			
Average	1.09	1.38	46.06	1.39	2.76	37.22	21.92	4.39	0.61	5.84	66.93	27.23
Deviation	0.05	0.75	3.24	0.80	1.06	21.62	8.45	0.90	0.28	0.00	0.00	0.00

2_02

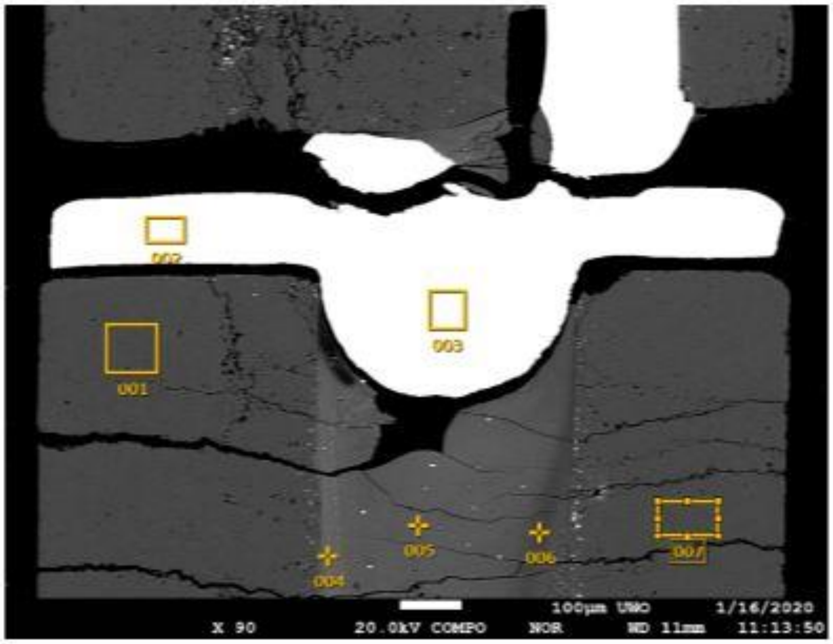

Volt : 20.00 kV
Mag. : x 90
Date : 2020/01/16
Pixel : 1280 x 960

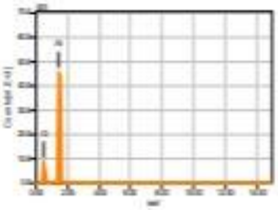
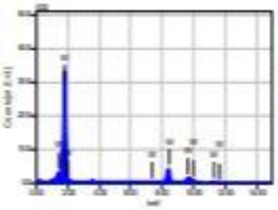
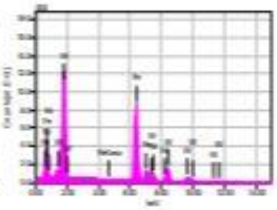

Acquisition Condition
Instrument : 8530F
Volt : 20.00 kV
Current : ---
Process Time : T2
Live time : 10.01 sec.
Real Time : 14.37 sec.
DeadTime : 30.00 %
Count Rate : 67321.00 CP

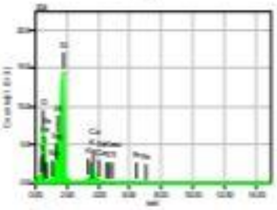
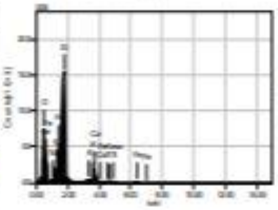
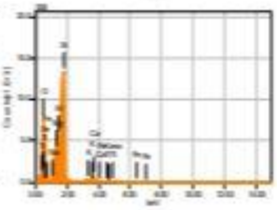
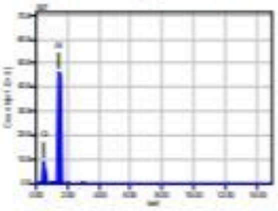

	Fe	K	O	Na	Mg	Al	Si	Ca	Ti	Ni	W
001			44.30			55.70					
002											100.00
003	47.68									6.18	46.14
004	2.37	1.18	51.05	0.53	4.00	9.51	25.17	5.50	0.69		
005	1.07	1.25	53.20	0.42	3.24	7.84	26.78	5.50	0.70		
006	1.65	1.04	52.13	0.69	6.75	9.76	24.97	2.29	0.72		
007			44.11			55.89					
Average	13.20	1.16	48.96	0.55	4.66	27.74	25.64	4.43	0.70	6.18	73.07
Deviation	23.00	0.10	4.40	0.13	1.85	25.62	0.99	1.86	0.01	0.00	38.09

Exp 3 (recovered from 3 GPa, 1930 K) - EDS

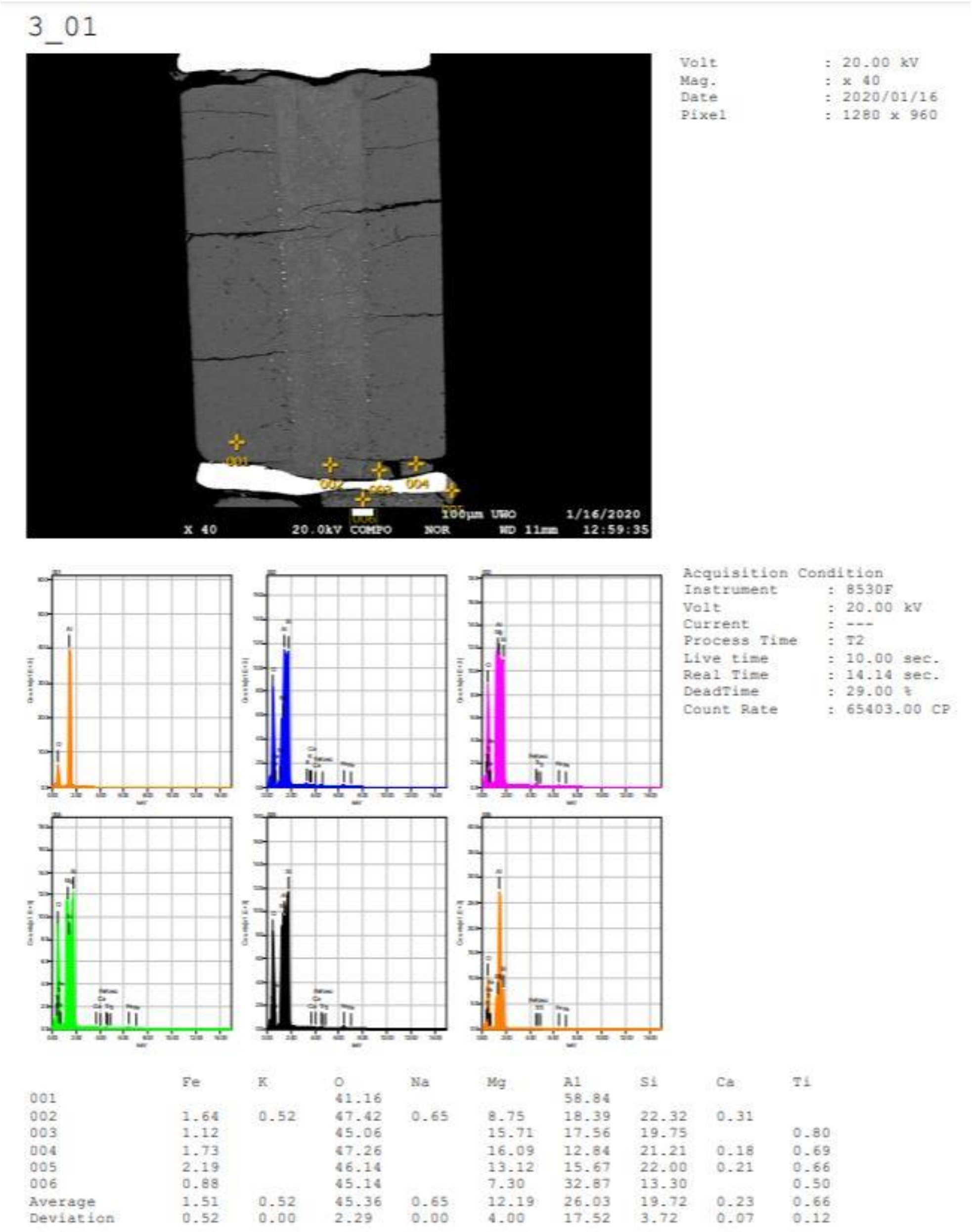

3_01

Volt : 20.00 kV
Mag. : x 40
Date : 2020/01/16
Pixel : 1280 x 960

Acquisition Condition
Instrument : 8530F
Volt : 20.00 kV
Current : ---
Process Time : T2
Live time : 10.00 sec.
Real Time : 14.14 sec.
DeadTime : 29.00 %
Count Rate : 65403.00 CP

	Fe	K	O	Na	Mg	Al	Si	Ca	Ti
001			41.16			58.84			
002	1.64	0.52	47.42	0.65	8.75	18.39	22.32	0.31	
003	1.12		45.06		15.71	17.56	19.75		0.80
004	1.73		47.26		16.09	12.84	21.21	0.18	0.69
005	2.19		46.14		13.12	15.67	22.00	0.21	0.66
006	0.88		45.14		7.30	32.87	13.30		0.50
Average	1.51	0.52	45.36	0.65	12.19	26.03	19.72	0.23	0.66
Deviation	0.52	0.00	2.29	0.00	4.00	17.52	3.72	0.07	0.12

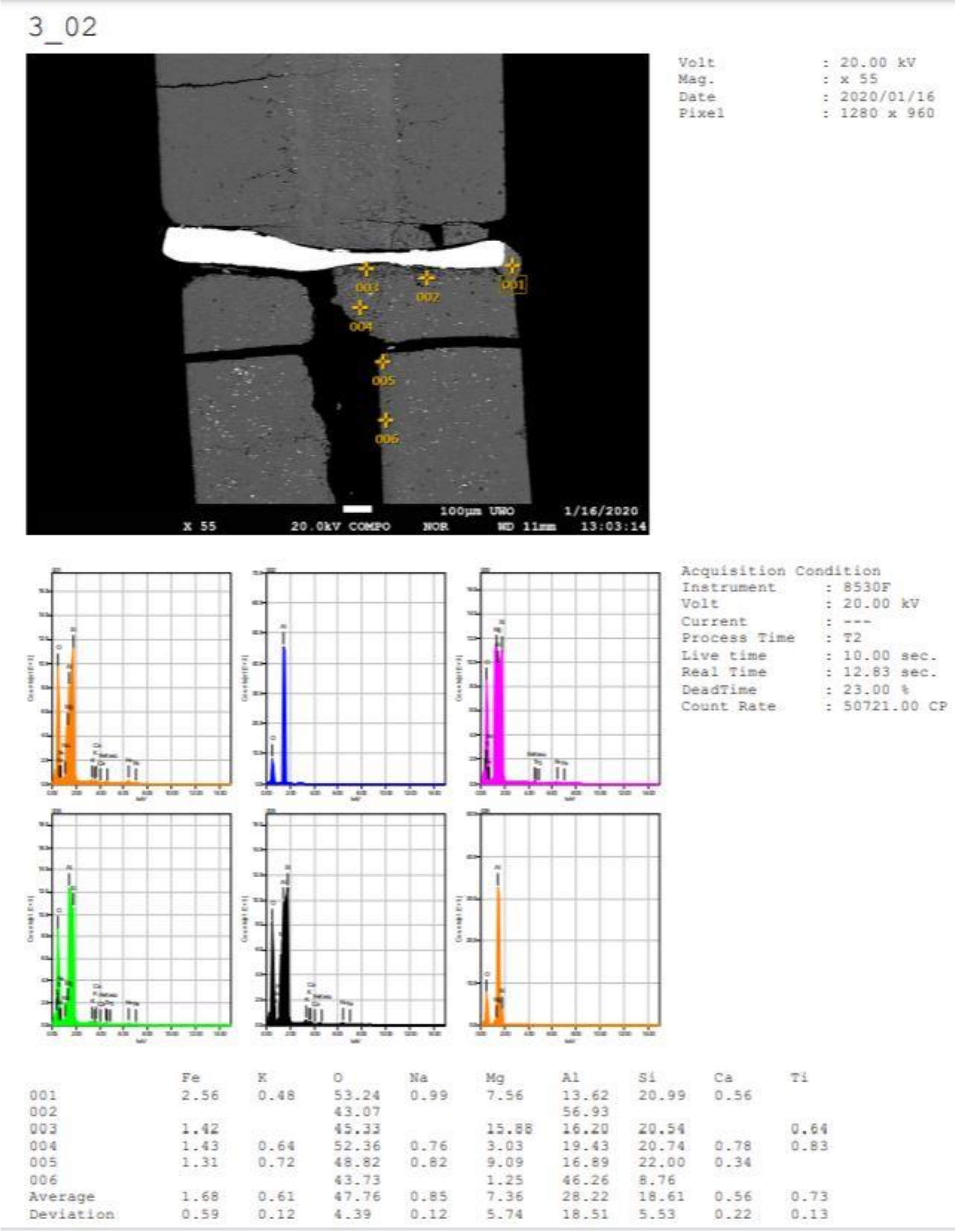

3_02

Volt : 20.00 kV
Mag. : x 55
Date : 2020/01/16
Pixel : 1280 x 960

Acquisition Condition
Instrument : 8530F
Volt : 20.00 kV
Current : ---
Process Time : T2
Live time : 10.00 sec.
Real Time : 12.83 sec.
DeadTime : 23.00 %
Count Rate : 50721.00 CP

	Fe	K	O	Na	Mg	Al	Si	Ca	Ti
001	2.56	0.48	53.24	0.99	7.56	13.62	20.99	0.56	
002			43.07			56.93			
003	1.42		45.33		15.88	16.20	20.54		0.64
004	1.43	0.64	52.36	0.76	3.03	19.43	20.74	0.78	0.83
005	1.31	0.72	48.82	0.82	9.09	16.89	22.00	0.34	
006			43.73		1.25	46.26	8.76		
Average	1.68	0.61	47.76	0.85	7.36	28.22	18.61	0.56	0.73
Deviation	0.59	0.12	4.39	0.12	5.74	18.51	5.53	0.22	0.13

Exp 5 (recovered from 5 GPa, 400 K) - EDS

5_eds1

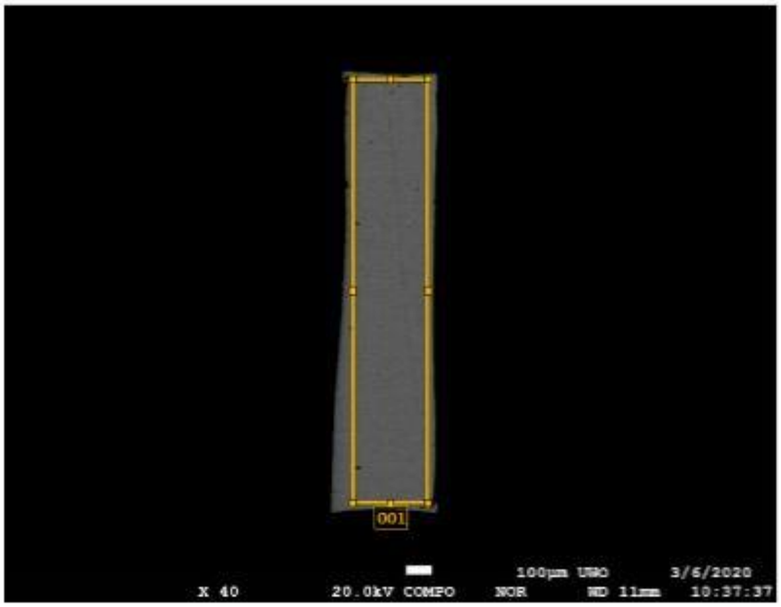

```
Volt             : 20.00 kV
Mag.             : x 40
Date             : 2020/03/06
Pixel            : 1280 x 960
```

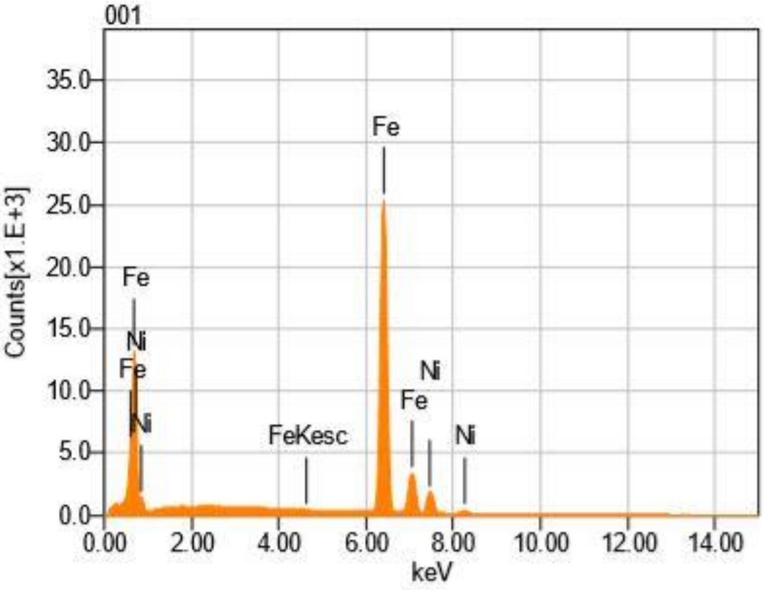

```
Acquisition Condition
Instrument         : 8530F
Volt               : 20.00 kV
Current            : ---
Process Time       : T2
Live time          : 60.01 sec.
Real Time          : 66.79 sec.
DeadTime           : 10.00 %
Count Rate         : 19604.00 CP
```

```
Formula          mass%    Atom%    Sigma    Net              K ratio           Line
Fe               89.58    90.03    0.02     13979942         48.1189742        K
Ni               10.42    9.97     0.01     1057148          5.0684760         K
Total            100.00   100.00
```

EXP 6 (recovered from 5 GPa, 1684 K) - EDS

6_eds1

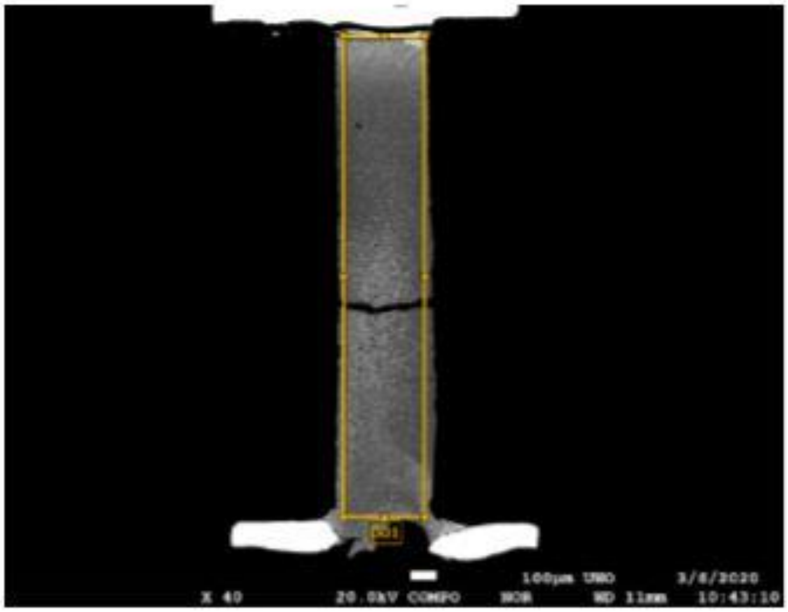

```
Volt            : 20.00 kV
Mag.            : x 40
Date            : 2020/03/06
Pixel           : 1280 x 960
```

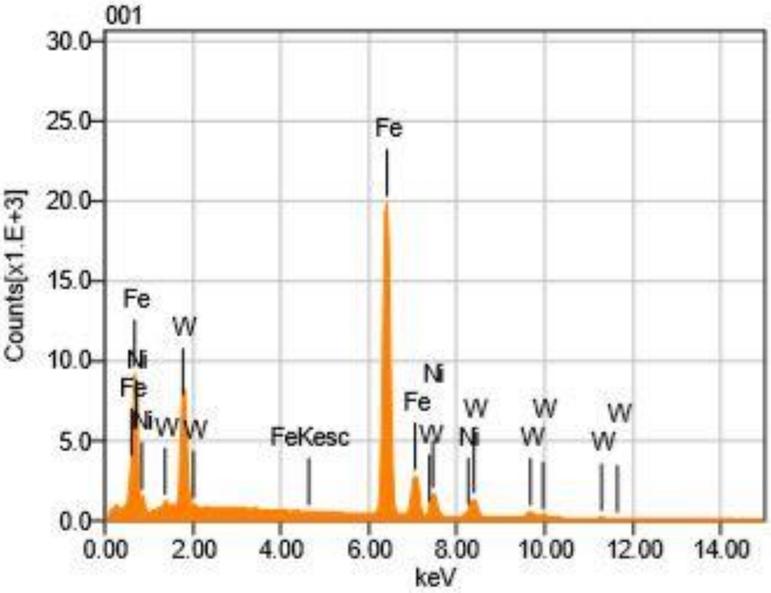

```
Acquisition Condition
Instrument      : 8530F
Volt            : 20.00 kV
Current         : ---
Process Time    : T2
Live time       : 60.00 sec.
Real Time       : 67.13 sec.
DeadTime        : 11.00 %
Count Rate      : 20223.00 CP
```

Formula	mass%	Atom%	Sigma	Net	K ratio	Line
Fe	70.41	83.11	0.02	10878312	37.4494021	K
Ni	8.22	9.22	0.01	855051	4.1002084	K
W	21.38	7.67	0.03	2839696	6.5121291	M
Total	100.00	100.00				